

PREDICTING GAIA'S PARALLAX DISTANCE TO THE CYGNUS OB2 ASSOCIATION WITH ECLIPSING BINARIES

DANIEL C. KIMINKI¹, HENRY A. KOBULNICKY², CARLOS A. VARGAS ÁLVAREZ^{2,3}, MICHAEL J. ALEXANDER^{2,4}, MICHAEL J. LUNDQUIST²

Draft version August 14, 2015

ABSTRACT

The Cygnus OB2 Association is one of the nearest and largest collections of massive stars in the Galaxy. Situated at the heart of the “Cygnus X” complex of star-forming regions and molecular clouds, its distance has proven elusive owing to the ambiguous nature of kinematic distances along this $\ell \simeq 80^\circ$ sightline and the heavy, patchy extinction. In an effort to refine the three-dimensional geometry of key Cygnus X constituents, we have measured distances to four eclipsing double-lined OB-type spectroscopic binaries that are probable members of Cyg OB2. We find distances of 1.33 ± 0.17 , 1.32 ± 0.07 , 1.44 ± 0.18 , and 1.32 ± 0.13 kpc toward MT91 372, MT91 696, CPR2002 A36, and Schulte 3 respectively. We adopt a weighted average distance of 1.33 ± 0.06 kpc. This agrees well with spectrophotometric estimates for the Association as a whole and with parallax measurements of protostellar masers in the surrounding interstellar clouds, thereby linking the ongoing star formation in these clouds with Cyg OB2. We also identify Schulte 3C (O9.5V), a $4''$ visual companion to the 4.75 day binary Schulte 3(A+B), as a previously unrecognized Association member.

Subject headings: Techniques: radial velocities — (Stars:) binaries: general — (Stars:) binaries: spectroscopic — (Stars:) binaries: (*including multiple*) close — Stars: early-type — Stars: kinematics and dynamics

1. INTRODUCTION

The Cygnus OB2 Association (also known as VI Cygni) harbors the largest number of O stars among nine OB associations within the “Cygnus X” (Piddington & Minnett 1952) complex, and it is one of the richest OB associations in the Galaxy. Cygnus X is a conspicuously bright region in radio, X-ray, and infrared maps of the Galactic Plane, covering nearly ten degrees near longitude $\ell=80^\circ$ (review by Odenwald & Schwartz 1993). Discovered as an overdensity of bright, reddened, early-type stars (Münch & Morgan 1953; Johnson & Morgan 1954; Schulte 1956, 1958), Cyg OB2 boasts ~ 60 O stars (Wright et al. 2015), perhaps as many as ~ 2600 B stars (Knöldseeder 2000), and some of the most massive stars known (Massey & Thompson 1991; Comerón et al. 2002). These are all veiled by heavy and variable interstellar extinction ($A_V = 4 - 12$ mag; Torres-Dodgen et al. 1991; Massey & Thompson 1991; Hanson 2003). In recent years, large surveys have produced an unprecedented panchromatic view of the interstellar environment that produced Cyg OB2. These include a five-band mid-infrared survey using the *Spitzer Space Telescope* (Beerer et al. 2010), maps of the molecular clouds in several CO transitions (Schneider et al. 2006; Leung & Thaddeus 1992), and maps of the dust continuum at 1.2 mm (Motte et al. 2007). O stars in Cyg OB2 were the first known stellar sources of X-ray emission (Harn-

den et al. 1979; Waldron et al. 1998), and several of the luminous members of the Association are prototypical examples for whole classes of massive star phenomena, such as the extremely luminous early-B supergiant Schulte 12 (MT91 314 in the numeration of Massey & Thompson 1991), the non-thermal radio source Schulte 9 (MT91 431; Abbott et al. 1984; Nazé et al. 2012), and the O3If* star Schulte 7 (MT457; Walborn 1973). As one of the nearest regions of massive star formation, Cyg OB2 also permits detailed investigations of OB stars and their interplay with the interstellar medium, such as the stellar bowshocks associated with high-velocity members (Comerón & Pasquali 2007; Gvaramadze 2007; Kobulnicky et al. 2010).

Despite its role as a nearby laboratory of massive star astrophysics, the distance to Cyg OB2 has proven elusive. In part, this is the result of variable extinction, which complicates spectrophotometric distances. Additionally, its location is at $\ell = 80^\circ$, where the relation between radial velocity and distance is not only double-valued but poorly-defined owing to velocity crowding along the tangent point of the local spiral arm (e.g., see Dame & Thaddeus 1985; Dame et al. 2001). Spectrophotometric distance measurements span a range that includes 1.5 kpc (Johnson & Morgan 1954), 2.1 kpc (Reddish et al. 1966), 1.7 kpc (Massey & Thompson 1991), 1.7 kpc (Torres-Dodgen et al. 1991), and 1.45 kpc (Hanson 2003). Additionally, studies of the eclipsing, double-lined spectroscopic binaries Cyg OB2-B17 (Stroud et al. 2010) and V382 Cyg (Yasarsoy & Yakut 2012) give distances of 1.5 – 1.8 kpc and 1.466 ± 0.076 kpc respectively. This range places Cyg OB2 within the local spiral arm or spur but is insufficiently precise for measuring key physical parameters such as luminosities and mass loss rates. Rygl et al. (2012) used radio-wave very-long-baseline interfer-

Electronic address: kiminki@email.arizona.edu

¹ Dept. of Astronomy, University of Arizona, 933 N. Cherry Avenue, Tucson, AZ 85721

² Dept. of Physics & Astronomy, University of Wyoming, 1000 E. University Avenue, Laramie, WY 82070

³ Physics Department, Hollins University, P.O. Box 9661, Roanoke, VA 24020

⁴ Dept. of Physics & Astronomy, Lehigh University, 27 Memorial Drive West, Bethlehem, Pennsylvania 18015, USA

ometry (VLBI) to measure parallaxes of five pre-main-sequence water and OH masers within Cygnus X and found that four of the five had distances between 1.3 and 1.5 kpc with typical uncertainties of 0.1 kpc. Zhang et al. (2012) also used VLBI techniques to measure a parallax distance of 1.61 ± 0.12 kpc to the red hypergiant NML Cygni, and they concluded that it may lie on the far side of the Cyg OB2 association. Dzib et al. (2012) reported radio VLBA observations giving a parallax distance of $1.65^{+0.96}_{-0.44}$ kpc to the colliding-wind binary Schulte 5, and they infer a probable distance of 1.3 – 1.4 kpc based on estimates of the orbital parameters in this quadruple system. While these parallax determinations are the most precise distances yet published, Cygnus X probably has a significant spread along the line of sight. Because of this, individual OB associations and star forming regions may lie anywhere within this depth. Thus, independent distance measurements of individual features are needed to help refine the line of sight structure of this complex, in particular for Cyg OB2.

In this contribution, we use four eclipsing double-lined spectroscopic binaries (SB2s) investigated as part of the Cygnus OB2 Radial Velocity Survey to calculate an independent distance to the Association. Papers I – VII in this series (Kiminki et al. 2007, 2008, 2009, 2012; Kiminki & Kobulnicky 2012; Kobulnicky et al. 2012, 2014) describe prior results of the Cygnus OB2 Radial Velocity Survey which measured the massive binary characteristics (i.e., binary fraction, distribution of periods, mass ratios, eccentricities) for more than 100 massive stars in a single cluster/association having a common formation environment. Paper V (Kiminki & Kobulnicky 2012), in particular, uses these basic data to infer the intrinsic distributions of massive binaries, concluding that: the fraction of massive stars having companions may be as high as 90%, 45% of these multiples are likely to interact at some point, there exists an excess of short-period 4 – 7 day systems relative to 7 – 14 day systems, and that unresolved secondaries contribute $\sim 16\%$ of the light in young stellar populations. Paper VII uses the extensive repository of orbital parameter information for the 48 known massive binaries to show that no single power law provides a statistically compelling prescription of the cumulative orbital period distribution, and that a flattening of the distribution at $P > 45$ d indicates either a lower binary fraction or a shift toward low-mass companions among long-period systems.

Our present dataset includes optical spectra and broadband photometry of four eclipsing double-lined spectroscopic binaries: MT91 372 and MT91 696 (nomenclature of Massey & Thompson 1991), CPR2002 A36 (nomenclature of Comerón et al. 2002, also known as RLP357 in Reddish et al. 1966), and Schulte 3 (nomenclature of Schulte 1958, also known as RLP920 in Reddish et al. 1966). Additionally, we make use of the Northern Sky Variability Survey (NSVS) photometry (Woźniak et al. 2004) for CPR2002 A36 and Schulte 3. In Paper III (Kiminki et al. 2009), we presented a single-lined orbital solution and NSVS photometry with a period of 2.22 days for MT91 372 (B2?+early B). Rios & DeGioia-Eastwood (2004) reported the SB2 (O9.5V+early B) nature of MT91 696 and estimated a photometric period of 1.46

d. A refined photometric period of 1.46919 ± 0.00006 d appears in Souza et al. (2014). We presented the first spectroscopic orbital solution in Paper IV with a similar period (Kiminki et al. 2012). Otero (2008a) identify the eclipsing nature of CPR2002 A36 using NSVS photometry. Its SB2 nature was noticed by Hanson (2003), and we presented the orbital solution for this $P=4.67$ d system in Paper III (Kiminki et al. 2009). Schulte 3 was discovered to be a double-lined (O6IV+O9III) spectroscopic binary with $P=4.74$ d in Paper II of this series (Kiminki et al. 2008). In this work, we analyze the light curve of this eclipsing system for the first time.

Section 2 of this work describes the new photometric and spectroscopic data obtained for the purpose of creating joint velocity curves and light curves for these four eclipsing double-lined systems. Section 3 reports the discovery of additional visual companions at small angular separations from Schulte 3 and MT91 696; knowledge of these third-light contributions is essential for accurate luminosities and distances. Section 4 provides details of the combined light-curve/velocity-curve modeling used to infer the distance to each system. Section 5 summarizes the new eclipsing binary distance to Cyg OB2 in relation to measurements of other targets in this region. All radial velocities reported here are in the Heliocentric reference frame.

2. OBSERVATIONS AND DATA REDUCTION

2.1. Spectroscopic Data

Optical spectroscopic observations of the four targets were obtained as part of the Cygnus OB2 Radial Velocity Survey on numerous dates between 2001 and 2011 using a variety of telescopes and instruments as described in Papers I – IV of this series. Several additional observations were obtained in 2012 October (on MT91 696 and Schulte 3) and 2013 May – June (on MT91 372) using the Wyoming Infrared Observatory (WIRO) Longslit spectrograph with an e2V 2048² CCD as the detector. A 2000 1 mm^{-1} grating in first order yielded a spectral resolution of 1.25 \AA near 5800 \AA with a $1.^{\prime\prime}2 \times 100''$ slit. The spectral coverage was $5250 - 6750 \text{ \AA}$. Exposure times ranged between 1200 s and 2 hours in multiples of 600 s depending on target brightness, current seeing ($1.^{\prime\prime}2 - 3''$ FWHM) and cloud conditions. Reductions followed standard longslit techniques, including flat fielding from dome quartz lamp exposures. Copper-argon arc lamp exposures were taken after each star exposure to wavelength calibrate the spectra to an rms of 0.03 \AA (1.5 km s^{-1} at 5800 \AA). Multiple exposures were combined yielding final signal-to-noise ratios (SNR) typically in excess of 100:1 near 5800 \AA . Final spectra were Doppler corrected to the Heliocentric velocity frame. Each spectrum was then shifted by a small additional amount in velocity so that the Na I D $\lambda\lambda 5890, 5996$ lines were registered with the mean Na I line wavelength across the ensemble of observations. This zero-point correction to each observation is needed to account for effects of image wander in the dispersion direction when the FWHM of the stellar point spread function was less than the slit width. Because of these inevitable slit-placement effects on the resulting wavelength solutions, radial velocity (RV) standards were not observed. Rel-

ative velocity shifts were generally less than 6 km s^{-1} , comparable to the magnitude of the random velocity uncertainties.

We measured an initial (final for CPR2002 A36) radial velocity for each spectrum obtained at WIRO using Gaussian fits to the He I $\lambda 5876$ line via the same method outlined in [Kobulnicky et al. \(2012\)](#), adopting a rest wavelength of 5875.69 \AA measured in model stellar spectra with static atmospheres (TLUSTY; [Lanz & Hubeny 2003](#); [Hubeny & Lanz 1995](#)). Our fitting code⁵ fixes the Gaussian width and depth at the mean value determined from all the spectra (after rejecting outliers), and it solves for the best-fit line center. In the case of an SB2, the code fits a double-Gaussian profile where the widths and depths have been fixed independently using observations obtained near quadrature orbital phases.

In this work, we used the initial radial velocities to disentangle the component spectra of MT91 372, MT91 696, and Schulte 3 using the method of [González & Levato \(2006\)](#).⁶ One of the strengths of this method is that the radial velocities can be refined via cross correlation after each iteration (i.e., cross-correlating the residual spectra with the resultant component spectrum as the template). The cross-correlated velocities generally have smaller uncertainties and utilize more lines, leading to a more precise measurement of the stellar velocity and the computed binary systemic velocity. Systemic velocities that are based solely on one hydrogen or helium line, such as He I $\lambda 5876$ with CPR2002 A36, may be blueshifted relative to the true systemic velocity owing to velocity contributions from strong winds. These contributions are strongest in very early-O stars and evolved stars. However, radial velocities for Schulte 3 are measured from many lines in the blue and red portions of the spectrum. The radial velocities of MT91 372 and MT91 696 are based on several hydrogen and helium lines between 5400 \AA and 6700 \AA and the stars are neither early-O or evolved.

Because of the more sophisticated approach to measuring the radial velocities in this work, the newly determined velocities will vary slightly from our previous works. This will be most evident for Schulte 3 and CPR2002 A36, which now have smaller O-C velocity residuals, indicating that a superior orbital solution has been obtained with the use of new data and methods. Table A.1 in the Appendix lists the Heliocentric Julian dates (column 1), orbital phase (column 2), radial velocities and uncertainties (columns 3 and 5), and the O-C residuals (columns 4 and 6) of each component for each of the four eclipsing SB2 systems.

2.2. Photometric Data

Photometry of MT91 696 was obtained on nine nights between 2012 October 17 and November 10 at the University of Wyoming 0.6 meter Red Buttes Observatory (RBO) using a 1024×1024 Apogee Alta U47 CCD through a V filter. Data on Schulte 3 was obtained on 14 nights at RBO between 2012 October 17 and 2012 December 21, and data on CPR2002 A36 was obtained

⁵ We use the robust curve fitting algorithm MPFIT as implemented in IDL ([Markwardt 2009](#)).

⁶ Disentangling is not performed for CPR2002 A36 on account of having an insufficient number of high-quality spectra.

on four nights between 2012 December 10 and 2012 December 22. The $0''.54 \text{ pixel}^{-1}$ scale at RBO yielded a $9.0'$ field of view centered on each object. Photometry of MT91 372 was also obtained at RBO on seven nights between 2013 June 14 and 2013 July 8 using an Alta U16 4096×4096 CCD binned 2×2 , yielding $0''.73$ pixels over a $24'$ field of view. The observations span 10 orbital periods of MT91 372, 16 orbital periods of MT91 696, two orbital phases of CPR2002 A36, and 13 orbital periods of Schulte 3. Seeing varied between $3''$ and $5''$ FWHM. Sky conditions were predominantly non-photometric. Sequences of 180 s, 120 s, and 30 s exposures were obtained for all systems, for several hours each night. Photometric conditions on 2012 October 18 (local) allowed us to obtain calibration images of several Landolt standard fields and fields in Cyg OB2 having UBV photometry in [Massey & Thompson 1991](#), (MT91). We elected to perform differential photometry using OB stars measured by [Massey & Thompson \(1991\)](#) in the V -band because of the lack of suitably red ($B - V > 1.2$) Landolt standards required to match the colors of the heavily reddened OB star targets. Additionally, we observed each target in the UBV filters on the (mostly) photometric night of 2012 December 09, interleaving target fields with nearby Cyg OB2 fields for purposes of tying our photometry to the MT91 UBV measurements.

RBO images were reduced using standard procedures which included removing the zero level with bias exposures, removing dark current using a median of at least seven dark exposures scaled to the appropriate target exposure time, and dividing by a normalized flat field constructed from the median of at least seven twilight sky exposures having a minimum of 10,000 electrons per image. We performed aperture photometry using IRAF/PHOT with an aperture of 14 pixels ($8''$) and a sky annulus extending from 14 to 19 pixels, in order to extract $> 99\%$ of the stellar flux for the target and 6 – 9 reference stars in each field. The magnitudes of the target stars were compared to the average of the comparison stars in each field to correct for (sometimes large) variations in atmospheric transmission. Differential photometry of MT91 372 used nine nearby field stars for reference, including four early type Cyg OB2 stars having similar color. The zero point of the photometric calibration relies upon stars from MT91 in the same field. The magnitudes of each comparison star were examined relative to the mean for the remainder of the stars, and in this way, we judge that the comparison stars were non-variable to the level of 0.015 mag over the course of our program. Photometric errors of the target star lie in the range 0.001 – 0.005 mag when considering only photon statistics as the dominant source of uncertainty. The exposure-to-exposure rms suggests that this is an appropriate estimate of the relative photometric uncertainty on any given night once brief time periods of heavy cloud cover were excised from the data. However, the rms difference of the comparison star mean magnitudes over all observing nights suggests that the night-to-night zero point is uncertain at the 0.010 mag level, which is small compared to the depth of eclipses over the orbital cycle.

For Schulte 3 and CPR2002 A36, we included the NSVS photometry ([Woźniak et al. 2004](#)) in addition to the RBO photometry. The NSVS photometry were taken with four Apogee AP-10 imaging cameras with an unfil-

tered optical response of $\sim 450 - 1000$ nm and an effective wavelength close to Johnson R-band. The data were collected over the course of one year, from 1999 April 1 through 2000 March 30 and exhibit an average photometric uncertainty of 0.01 mag. The NSVS data used here are converted from Modified-Julian Date (MJD) to Julian Date (JD).

Tables A.2 – A.5 in the Appendix list the Heliocentric Julian date and the V-band magnitudes of the MT91 372, MT91 696, CPR2002 A36, and Schulte 3 systems. Column 1 gives the Heliocentric Julian dates minus 2,400,000, while columns 2 and 3 list the V-band magnitudes and 1σ uncertainties calculated from photon statistics only. Additional uncertainties at the level of 0.010 mag are present as a result of uncorrected atmospheric transparency variations over the field of view and night-to-night zero point uncertainties. Only the first ten table lines are given to provide context and format. The full table appears in the *electronic edition* as a machine-readable table. The Schulte 3 photometry includes the contribution from the blended tertiary Schulte 3C discussed in the next section. Additionally, the data have been averaged into 2-minute intervals from the original 30-second exposure times. MT91 696 photometry also includes a contribution from the blended tertiary MT91 696C, discussed in the next section.

3. VISUAL COMPANIONS TO SCHULTE 3 AND MT91 696

3.1. Schulte 3C

Photometry of the double-lined eclipsing binary Schulte 3 was complicated by the presence of a nearby companion at $3.^{\circ}9$ separation at position angle 215° from the brightest visual component. Schulte 3 (comprised of 4.74 d eclipsing components “A” and “B”) and the companion, Schulte 3C, are blended in all of our RBO images, so our photometry using large apertures encompasses all stars. The companion is readily visible in UKIDSS Galactic Plane Survey images (Lucas et al. 2008) at R.A.=20:31:37.31 Declination=+41:13:17. (J2000), but both Schulte 3(A+B) and Schulte 3C are saturated. The companion is not present in the 2MASS Point Source Catalog because of blending. It is not visible in the Digitized Sky Survey for the same reason. We therefore conducted our own V-band imaging using the CCD guide camera on the WIRO-Longslit spectrograph ($0.^{\prime}147$ pixel $^{-1}$) on the night of 2012 November 06. Several 3 s exposures were obtained in $1.^{\prime}4$ seeing within a few minutes of JD=2456238.55 (2012 Nov 7, 01:19 UT). Figure 1 shows a greyscale representation of our V-band images, illustrating the relative locations of Schulte 3(A+B) and Schulte 3C. Photometry using these images indicates a magnitude difference $\Delta m_V = 2.14$ mag, meaning that Schulte 3(A+B) contribute 88% of the flux at V band, compared to 12% for Schulte 3C. Given a mean magnitude of $V=10.30 \pm 0.02$ on this date, derived from the phased light curve of Schulte 3 (§4.5), the companion has $V \approx 12.42 \pm 0.03$. It also means the third-light-adjusted V-band maximum (between primary and secondary eclipse) for the Schulte 3(A+B) system, as derived from the phased light curve, is 10.31 mag.

We obtained spectra of Schulte 3(A+B) and Schulte 3C using the WIRO Longslit spectrograph on the night of

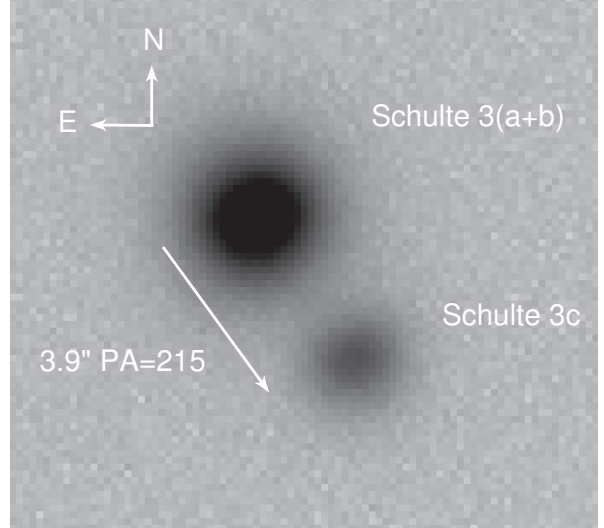


FIG. 1.— Greyscale image of Schulte 3 (the eclipsing double-lined components a+b) and its \sim O9.5V companion, Schulte 3C.

2012 October 21 in $2''$ seeing. Figure 2 plots the spectra of both components and labels some key spectral features of hot stars. The spectrum of Schulte 3C exhibits both He II $\lambda 5411$ and He I $\lambda 5876$ in the ratio $EW_{5411}/EW_{5876} \sim 0.4$, consistent with a temperature class near O9.5 (Kobulnicky et al. 2012). H α appears in absorption. The combination of the spectral characteristics and the V-band magnitude are both consistent with an O9.5V at the distance of Cyg OB2. With the current data it is not possible to say whether the companion is physically associated with Schulte 3, although the strong similarity of the many diffuse interstellar features in the two spectra make it likely that they both lie at a similar distance. If associated, Schulte 3 is a triple stellar system with Schulte 3C at a projected separation of about 5200 AU.

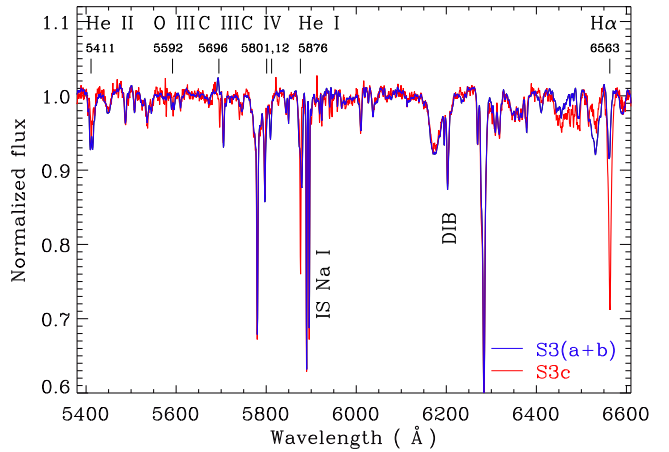


FIG. 2.— Spectra of the O6V+O9III double-lined system Schulte 3(A+B) (blue) and its $4''$ O9.5V companion, Schulte 3C (red). Labels mark key stellar features. Other features are interstellar. The excellent agreement between the interstellar features of both stars are consistent with a common distance. The two stars differ most notably in their He I $\lambda 5876$ and H α line depths, reflecting the higher effective temperature of Schulte 3(A+B).

In the analysis that follows, we assume, but do not have the data to demonstrate, that Schulte 3C is non-variable, both photometrically and spectroscopically. We are confident that it cannot be the source of the photometric variability, detailed in the next section because the spectroscopic period of Schulte 3(A+B), as observed in isolation, matches the photometric period observed for the whole system. However, the present data do not rule out the possibility that Schulte 3C may be a multiple subsystem or may be photometrically variable.

3.2. MT91 696C and 696D

While no similarly bright companions are seen in UKIDSS images for MT91 696, measurements with the *Hubble Space Telescope* Fine Guidance Sensors (FGS) (Caballero-Nieves et al. 2014) reveal two astrometric companions at $0''.023$ (MT91 696C) and $0''.84$ (MT91 696D) separations. A Cyg OB2 distance of 1.33 kpc implies minimum projected physical separations of 31 AU and 1117 AU respectively, indicating that this is likely a triple (possibly quadruple) system composed of a spatially unresolved 1.4 day binary (components A & B) and two additional components (C & D). With $\Delta m=0.94\pm0.40$ mag in the *HST* F583W bandpass, MT91 696C is the dominant source of excess light (MT91 696D is several magnitudes fainter), so we consider only this component in subsequent analysis of the light curve. The magnitude of MT91 696C would make it a probable mid-B star. As with Schulte 3, we assume, but do not have the data to demonstrate, that MT91 696C is non-variable, both photometrically and spectroscopically. It is also not the source of photometric variability for the same reasons as Schulte 3C. Lastly, while we consider photometric contamination from MT91 696C, we assume negligible radial velocity contamination given a computed semi-amplitude of $\sim 5.5 \text{ km s}^{-1}$ and total flux contribution of $\sim 14\%$ (see Section 4.4).

4. ANALYSIS OF ECLIPSING BINARIES

4.1. Modeling the Joint Light Curves and Velocity Curves

In general, effective temperatures for the primary star, T_1 , were held as fixed parameters based on the ratio of equivalent widths He II $\lambda 5411/\text{He I } \lambda 5876$ in our spectra. Figure 3 plots this EW ratio versus temperature as measured in Tlusty NLTE model atmosphere spectra (Lanz & Hubeny 2003) and CMFGEN model spectra (Hillier & Miller 1998)⁷ for four values of $\log(g)$, 4.0 – 3.25 (appropriate for luminosity classes V – I). Between $T=30,000$ K and $\sim 35,500$ K there is a nearly linear relationship between EW ratio and temperature. The solid line is a fit to the $\log(g)=4.0 - 3.75$ models over the range $T=27,500 - 40,000$ K, and the dashed line is a fit to the models with $\log(g)=3.25 - 3.50$ over the range $T=27,500 - 37,500$ K. Above these maximum temperatures, the linear relation becomes a poor approximation. Labels near the top of the panel give the corresponding spectral type according to the observational calibration of Martins et al. (2005) for dwarf and supergiant luminosity classifications.

⁷ As measured from the grid of O star stellar models dated 2009 June 24 from the webpage of J. Hillier, <http://kookaburra.phyast.pitt.edu/hillier/web/CMFGEN.htm>.

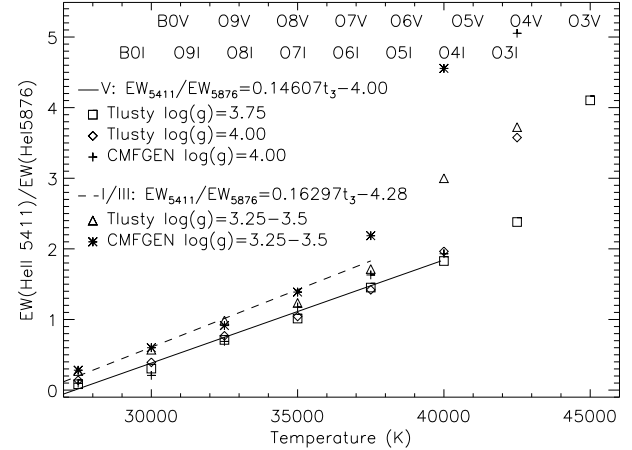


FIG. 3.— Relation between equivalent width ratio He II $\lambda 5411/\text{He I } \lambda 5876$ versus temperature based on Tlusty Lanz & Hubeny (2003) and CMFGEN (Hillier & Miller 1998) NLTE model atmospheres for values of $\log(g)$ appropriate to main-sequence (3.75 – 4.0) and giant/supergiant (3.25 – 3.5) late-O and early B stars. The expressions within the panel quantify this quasi-linear relationship over the range 27,500 K – 37,500 K for luminosity class V stars (solid line) and 27,500 K – 35,000 K for luminosity class I/III stars (dashed line), where t_3 is temperature in 10^3 K.

To obtain the most probable orbital period, we examined each component's CLEANed radial velocity power spectrum using an IDL⁸ program written by A. W. Fullerton, which makes use of the discrete Fourier transform and CLEAN deconvolution algorithm of Roberts et al. (1987). Sufficient radial velocity and light curve data exist for each system so that periods are secure and free of aliases. Spectroscopic solutions were then computed with the Binary Star Combined Solution Package, BSCSP (Gudehus 2001). The spectroscopic orbital parameters determined from BSCSP were used as initial parameters within the eclipsing binary package, PHOEBE (Prša & Zwitter 2005), which is based on the code of Wilson & Devinney (1971), to model the joint light curves and radial velocity curves. For the light curve parameters, we chose albedos and gravity darkening coefficients appropriate for radiative atmospheres (1.0) and limb darkening coefficients interpolated from van Hamme (1993). Gravity darkening and albedo were treated as fixed parameters. We allowed each system one reflection from the opposite star and used the Kurucz atmospheric models as the description of the star's wavelength-dependent emergent flux (Kurucz 1979).

We selected the appropriate PHOEBE geometrical configuration for each system based on the shape of the light curve (i.e., double-contact for CPR2002 A36 and Schulte 3, and detached for both MT91 372 and MT91 696). Including only the spectroscopic data for each system, we used PHOEBE's differential correction method to refine the spectroscopic solution while allowing period, eccentricity, separation, epoch of periastron, angle of periastron, systemic velocity, and mass ratio to vary. From this point, for the detached systems, we determined the roughly optimized photometric solution by varying inclination, surface potential, luminosity, and

⁸ The Interactive Data Language (IDL) software is provided by Exelis Visual Information Solutions.

secondary temperature, using only the photometric data. Schulte 3 and CPR2002 A36 show evidence of hot spots on the secondary component via the O'Connell effect in their light curves⁹, Struve-Sahade effect¹⁰ in their He I lines, and complex varying H α emission. For the model of these two systems, we added one spot to the secondary and manually adjusted the spot temperature, size, and location in an iterative process with the differential corrections to obtain the roughly optimized solution. Despite the evidence pointing to the spot being associated with the secondary (discussed in Sections 4.5 and 4.6), we also attempted placing the spot on the primary. For both systems, the spot on the secondary provided the better fit to the data. The spot parameters were adjusted manually because of the degenerate nature of the solutions (i.e., spot size, spot temperature, and stellar effective temperature are degenerate when the analysis is limited to 1 – 2 photometric bandpasses).

Once refined solutions for both the photometric and spectroscopic data were obtained separately, we optimized the ephemeris by using all data and varying the period and epoch of periastron. The eccentricity and angle of periastron were held fixed for MT91 696, CPR2002 A36, and Schulte 3, but varied for MT91 372. Finally, we obtained our best-fit solution by varying the remaining variables that depend on both spectroscopic and photometric data (i.e., inclination, separation, and relative luminosities). Owing to uncertainties on the primary component temperatures, a small grid of solutions was computed for a range of plausible T_1 values. When a final orbital solution was obtained, we compared the results with those obtained using `Nightfall`, an eclipsing binary package created by Rainer Wichmann¹¹ and based on the [Wilson & Devinney \(1971\)](#) code assuming typical Roche geometry. All results from `Nightfall` were consistent with `PHOEBE` within our final uncertainties. We obtained formal parameter uncertainties via the instructions in the `PHOEBE` manual, where fit parameter uncertainties come from the covariance matrices and derived parameter uncertainties are calculated via propagation of error. We note that the solutions of Schulte 3 and CPR2002 A36 suffer degeneracies stemming from probable hot spots and being limited to 1-2 bandpasses. Further discussion of these degeneracies are provided in Sections 4.5 and 4.6.

`PHOEBE` solutions provide computed theoretical absolute bolometric magnitudes. However, because the bolometric magnitudes represent the components only, rather than the components and additional spots, we estimated the apparent magnitude for Schulte 3 and CPR2002 A36 from the model by turning off the spot contribution once a solution was finalized. We then used bolometric correc-

⁹ The O'Connell effect is defined as the unequal out-of-eclipse maxima ([O'Connell, D. J. K. 1951](#)). Many likely causes have been proposed for the phenomenon, but for W Uma systems the probable cause is a hot spot resulting from a mass stream between the two components.

¹⁰ The Struve-Sahade is defined as the variation in a component's spectral profiles as a function of phase. The equivalent width of the lines may or may not vary, and the effect can affect all lines or a few. Helium absorption lines are often affected, and the effect is generally associated with the secondary. [Linder et al. \(2007\)](#) and [Bagnulo et al. \(1999\)](#) provide a good summary with examples.

¹¹ <http://www.hs.uni-hamburg.de/DE/Ins/Per/Wichmann/Nightfall.html>

tions interpolated from the tables of [Martins et al. \(2005\)](#) and the PARSEC isochrones ([Bressan et al. 2012](#)) to determine the absolute visual magnitudes. The distance to each system may then be derived using the resulting distance modulus in conjunction with an estimate of the extinction, A_V (§4.2).

4.2. Extinction Calculations

We estimate the extinction toward each system from the $UBVJHK$ broadband photometry, compiled in Table 1 from published sources and from our own UBV photometry, in conjunction with an adopted spectral energy distribution from [Kurucz \(1992\)](#) atmospheres of the appropriate T_{eff} and $\log(g)$ for its spectral type. The JHK photometry are drawn from the Two-Micron All Sky Survey (2MASS) Point Source Catalog¹², while UBV measurements come from various independent sources. We redden the model atmosphere by either a [Cardelli et al. \(1989, CCM89\)](#) or a [Fitzpatrick & Massa \(2007, FM07\)](#) prescription for interstellar extinction. [Cardelli et al. \(1989\)](#) provide an analytical description of the average interstellar extinction law over the ultraviolet, optical and near-infrared range, parameterized in terms of two variables, A_V and R_V . [Fitzpatrick & Massa \(2007\)](#), by contrast, present a table of 328 discrete reddening curves toward individual Galactic sources; they highlight the uniqueness of each sightline, stressing how generalized curves such as [Cardelli et al. \(1989\)](#) are gross averages over diverse interstellar dust components. We fit reddened photospheres to the data for each star using each of these prescriptions. Table 1 the best-fit A_V and R_V values. Our approach is more fully described in [Vargas-Álvarez et al. \(2013\)](#), who find good agreement between these two descriptions of extinction toward the heavily reddened Galactic cluster Westerlund 2. They note how the non-standard value of $R_V=3.8$ along that sightline results in a significantly smaller distance than if the canonical $R_V=3.1$ were adopted.

Because these targets are variable at the level of 0.5, 0.6, 0.3, and 0.5 mag level for MT91 372, MT91 696, Schulte 3, and CPR2002 A36 respectively, a robust reddening solution ostensibly depends on acquiring UBV and JHK datasets at the same orbital phase. The 2MASS JHK observations were made simultaneously at orbital phase, $\phi=0.74$, 0.84, 0.69, 0.68 for MT91 372, MT91 696, CPR2002 A36, and Schulte 3, respectively, assuming that the orbital periods have remained constant since the 1998 June 2MASS observations. The times of observation are not available in published sources for the majority of the UBV photometry, except for our new data presented here which we acquired at orbital phase $\phi=0.32$ and 0.47 for MT91 696 and Schulte 3, respectively, near JD=2456271.58 early on 2012 December 10 (UT). Assuming that the orbital periods have remained constant and that the broadband colors remain unchanged throughout the eclipse cycle (a plausible assumption given the similarity in temperatures between

¹² Because of the low angular resolution of 2MASS, there may be flux contributions from unresolved components. However, only in the case of Schulte 3 is there a tertiary bright enough and close enough to be considered significant (12% of the system light), and even this contribution is inconsequential to the reddening results because of the very large extinctions.

components in all cases), we correct our *UBV* photometry to the orbital phase of the 2MASS photometry before fitting for the optimal reddening solution. These corrected values are listed and footnoted as such in Table 1. In practice, we find that the reddening toward all targets is sufficiently large that adjusting photometry to a common orbital phase is a small correction compared to the $A_V > 5$ mag interstellar contributions to the broadband magnitudes. Hence, these corrections make negligible difference on the final reddening parameters.

The *UBV* photometry reported in the literature for a given system shows dispersion beyond the formal uncertainties ($0.01 - 0.03$ mag based on published sources), consistent with data being obtained at different orbital phases and/or real intrinsic variations in the luminosity of the sources. Furthermore, MT91 note the systematic differences between their *UBV* photometry and that of Reddish et al. (1966). For purposes of chi-squared minimization, we adopt somewhat generous uncertainties of $0.05, 0.05, 0.03, 0.01, 0.01, 0.01$ mag on the *UBVJHK* photometry, respectively.

Table 1 lists the photometry and best-fit reddening parameters A_V and R_V for each combination of *UBV* measurements, paired with the 2MASS *JHK* photometry, for both the CCM89 and FM07 reddening curves. Inspection of the individual values reveals generally good agreement between the reddening parameters computed using different datasets and the same reddening law. For example, the extinction results using CCM89 for MT91 372 are $A_V = 7.15$ and 7.03 mag for the two available *UBV* datasets, giving a mean of 7.09 . The results using the FM07 reddening curves are $A_V = 7.01$ and 7.13 mag. The means of $A_V = 7.09$ and 7.07 mag, respectively, for the CCM89 and the FM07 curves are nearly identical. The results using CCM89 for MT91 696 are $A_V = 5.82, 6.30$, and 5.83 with a mean of 5.98 . The results using the FM07 reddening curves are $A_V = 5.88, 5.94$, and 5.75 with a similar mean 5.85 . CPR2002 A36 and Schulte 3 have mean reddenings of $A_V = 6.74$ and 6.07 mag, respectively, using the CCM89 reddening curve and $A_V = 6.46$ and 6.02 mag, respectively, using the FM07 curves. We conclude that there is good agreement between the extinctions derived using either the MT91 *UBV* photometry in conjunction with 2MASS *JHK* and our own photometry with 2MASS. There is also good agreement between the extinctions derived for MT91 372, MT91 696 and Schulte 3 (dispersions ~ 0.1 mag) using the two reddening curves, but the dispersion is somewhat larger for CPR2002 A36, leading to a larger uncertainty on A_V .

Finally, we note that the best-fit FM07 reddening curves have reduced chi-squared values in the range $1 - 10$ while those for the CCM89 parameterization have much larger reduced chi-squared values of $7 - 50$. We adopt 4 degrees of freedom for the 6 data points in each case, although this is not strictly correct for FM07 because these curves are fitted empirical characterizations rather than parameterizations. Nevertheless, the FM07 series of curves always provides a better fit to the data than the average curve of CCM89.¹³ The fitting process consistently selects curves from the FM07 library

¹³ The Cygnus region may have an anomalous reddening curve (Turner 1989) so the CCM89 average parameterization could be less applicable along this sightline.

corresponding to early type stars from NGC 6530, suggesting that this sightline produces reddening similar to that of the dust toward Cyg OB2. The mean extinction and reddening of the FM07 fits for MT91 372 are 7.07 ± 0.12 mag and 3.37 ± 0.44 , respectively. For MT91 696, the FM07 fits yield means of $A_V = 5.85 \pm 0.09$ mag and $R_V = 3.30 \pm 0.20$, and this extinction estimate compares favorably to the $A_V = 5.84$ mag found by Massey & Thompson (1991), despite their assumption of $R_V = 3.0$. The mean of the FM07 fits for CPR2002 A36 provide $A_V = 6.46 \pm 0.23$ mag and $R_V = 3.42 \pm 0.19$. And finally, for Schulte 3 we find $A_V = 6.02 \pm 0.09$ mag and $R_V = 3.19 \pm 0.23$, which is slightly smaller than the $A_V = 6.24$ mag found by Torres-Dodgen et al. (1991). Torres-Dodgen et al. (1991) determined $R_V = 3.04 \pm 0.09$ for dozens of stars in the Cyg OB2 vicinity. Our average value using the CCM89 reddening curve is $R_V \simeq 3.05 \pm 0.05$, whereas our average value using FM07 is $R_V \simeq 3.3 \pm 0.1$, somewhat higher but consistent with values found throughout the region. Hereafter, we adopt the best-fit FM07 extinction fits. We note that adoption of the CCM89 reddening law would systematically lower the derived distance modulus for CPR2002 A36 by about 0.28 mag, but it will have a very small impact on the distances for MT91 372, MT91 696 and Schulte 3.

4.3. MT91 372

Of the four eclipsing systems analyzed, MT91 372 is one of the most ideal for determining distance. Figure 4 shows the velocity curve data and best-fit model (top), light curve and best-fit model (middle), and light curve residuals (bottom). The components are detached with clear, deep eclipses having $\Delta m \simeq 0.2$ for the secondary eclipse and $\Delta m \simeq 0.5$ for the primary eclipse in V. Figure 5 shows disentangled spectra for each component. The primary star displays strong He I $\lambda 5876$ lines relative to H α , indicative of a hot star in the range B0V – B2V. While He I is present in the secondary, this ratio is smaller, indicating a later spectral type near mid-B.

Because this system is among the faintest and reddest objects in the Cygnus OB2 Radial Velocity Survey ($V = 14.96$ at its brightest and $A_V \simeq 7$ mag), the SNR of the Survey's WIYN spectra are insufficient to use the well-calibrated EW_{4481}/EW_{4471} ratios to measure component temperatures. We determine a 2σ upper limit of $T_1 < 28,000$ K for the primary based on an upper limit for the ratio $EW_{5411}/EW_{5876} < 0.10$ (calibrated using Figure 3) in a combination of all available WIRO spectra taken near the same quadrature phase.¹⁴ The available spectra provide no strong lower limits on the effective temperature of the primary. The presence of He I $\lambda 5876$ with an EW of 0.60 ± 0.02 Å in the separated primary star spectrum in Figure 5 confirms that MT91 372a is a hot star with $T_1 > 18,000$ K based on the calibration

¹⁴ The measured (indicated by subscript m) equivalent widths of lines in a composite spectrum of two stars, $EW_{m,1}$ and $EW_{m,2}$, yield the true (indicated by subscript t) equivalent widths via the ratio of continuum light at that wavelength, $l \equiv C_1/C_2$, as $EW_{t,1} = EW_{m,1}(1+l)/l$ and $EW_{t,2} = EW_{m,2}(1+l)$ (Hilditch 2001, eqn. 5.98). However, assuming that the continuum light ratios of the two very hot stars at 5876Å is the same as at 5411Å, a direct measurement of the ratio EW_{5411}/EW_{5876} for each star is essentially independent of l .

TABLE 1
 A_V AND R_V ESTIMATES

Quantity	MT91 372	MT91 696	CPR2002 A36	Schulte 3
U	18.01 ^a	14.44 ^a	13.73 ^c	12.31 ^c
B	17.14 ^a	13.97 ^a	12.78 ^c	11.85 ^c
V	14.97 ^a	12.32 ^a	11.36 ^c	10.09 ^c
J	12.51 ^b	8.53 ^b	7.19 ^b	6.50 ^b
H	9.92 ^b	8.14 ^b	6.65 ^b	6.00 ^b
K	9.60 ^b	7.89 ^b	6.36 ^b	5.74 ^b
A_V (CCM89)	7.15	5.82	6.63	6.16
R_V (CCM89)	3.03	2.90	3.11	3.11
A_V (FM07)	7.01	5.88	6.56	5.92
R_V (FM07)	2.93	3.06	3.31	2.93
U	17.19	14.20 ^c	13.73 ^c	12.30 ^e
B	16.52	13.87 ^c	12.81 ^d	11.83 ^e
V	15.04	12.36 ^c	11.27 ^d	10.22 ^e
A_V (CCM89)	7.03	6.30	6.96	5.93
R_V (CCM89)	2.95	3.11	2.92	2.92
A_V (FM07)	7.13	5.94	6.46	6.07
R_V (FM07)	3.81	3.42	3.31	3.30
U	...	14.00 ^f	13.19 ^f	12.12 ^f
B	...	13.69 ^f	12.77 ^f	11.77 ^f
V	...	12.20 ^f	11.15 ^f	10.22 ^f
A_V (CCM89)	...	5.83	6.63	6.13
R_V (CCM89)	...	2.98	3.02	3.02
A_V (FM07)	...	5.75	6.36	6.09
R_V (FM07)	...	3.42	3.64	3.36
Avg. A_V (CCM89)	7.09 \pm 0.12	5.98 \pm 0.27	6.74 \pm 0.19	6.07 \pm 0.12
Avg. R_V (CCM89)	2.99 \pm 0.08	3.00 \pm 0.10	3.09 \pm 0.10	3.02 \pm 0.09
Avg. A_V (FM07)	7.07 \pm 0.12	5.85 \pm 0.09	6.46 \pm 0.23	6.02 \pm 0.09
Avg. R_V (FM07)	3.37 \pm 0.44	3.30 \pm 0.20	3.42 \pm 0.19	3.19 \pm 0.23

^a Massey & Thompson (1991)

^b 2MASS; data acquired at orbital phase $\phi=0.74, 0.84, 0.69, 0.68$ for MT91 372, MT91 696, CPR2002 A36, and Schulte 3, respectively, assuming that the orbital periods have remained constant since the 1998 2MASS observation.

^c Reddish et al. (1966)

^d Tycho-2 Høg et al. (2000)

^e Nicolet (1978)

^f This work; obtained at orbital phase $\phi=0.32, 0.49, 0.47$ for MT91 696, CPR2002 A36, and Schulte 3, respectively We have corrected our measured UBV magnitudes to the same orbital phase as the 2MASS JHK measurements using the derived orbital solution under the assumption of constant orbital periods and constant broadband color.

between T_{eff} and He I $\lambda 5876$ presented in Figure 3 of Kobulnicky et al. (2012). The ratio $EW_{6563}/EW_{5876} \simeq 5$ provides similar loose constraints.

In an attempt to provide a more secure lower limit on the effective temperature of the primary, MT91 372 was observed at WIRO on 2013 August 14 and August 29 for 3 hours (12×900 s) each using a 2000 l mm^{-1} grating in first order over the wavelength range $6900 - 8000\text{ \AA}$. The dates of observation were chosen to cover portions of the orbital phase (0.09 and 0.85, respectively) where the temperature-sensitive far-red lines of He I $\lambda 7065$, O I $\lambda\lambda 7772, 7774, 7775\text{ \AA}$, and Mg II $\lambda 7896$ fell at locations minimally affected by atmospheric absorption, interstellar bands, and night sky emission lines. No order blocking filter was used as the atmosphere, detector, and heavy interstellar extinction ($A_V = 7$ mag) effectively serve to block wavelengths shorter than 4000 \AA . Data reduction followed standard procedures described in Section 2. Particular care was taken with the continuum normalization of the spectra to ensure that line-free portions were used to fit a low-order polynomial to the spectrum. Regions of strong atmospheric absorption near $7150 - 7400\text{ \AA}$ and $7600 - 7700\text{ \AA}$ were excluded from

the fit. From these spectra we detect He I $\lambda 7065$ at the expected level for stars between $20,000$ K and $28,000$ K, but O I $\lambda\lambda 7772, 7774, 7775\text{ \AA}$, and Mg II $\lambda 7896$ lines are not detected to upper limits of $\sim 0.12\text{ \AA}$. While this limit does not place useful constraints on the temperature on the basis of the expected Mg II $\lambda 7896$ equivalent widths (0.05 \AA or less for stars hotter than $20,000$ K, based on Tlusty models), the limits are useful in the case of the O I $\lambda\lambda 7772, 7774, 7775$ blend which ought to have a combined $EW > 0.2\text{ \AA}$ for stars cooler than $20,000$ K.

We conclude that $20,000$ K is a secure lower limit on T_1 . Accordingly, we adopt a temperature of $24,000 \pm 3,000$ K for the primary component, MT91 372a. Given that the system is clearly detached with a small separation, the components are not likely filling their Roche lobes. Based on the absence of emission features we assume that the components are un-evolved. The joint light curve and velocity curve analysis to follow confirms that the components have radii consistent with main-sequence, early B stars.

Radial velocities obtained from WIRO-Longslit spectra between 2008 and 2013 (12 epochs for the primary, 11 epochs for the secondary) produce power spectra with

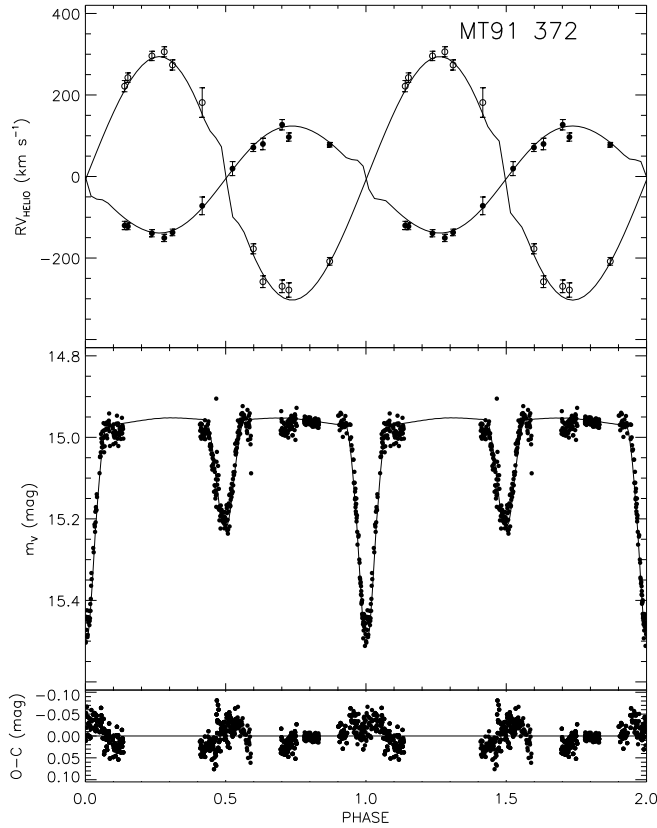


FIG. 4.— Radial velocity curve (top), light curve (middle), and light curve residuals (bottom) for MT91 372. Solid and unfilled points (top) denote the primary and secondary radial velocities, respectively. Solid curves in each panel show the best-fit PHOEBE solutions given the adopted parameters, as described in the text. The steps at phases of 0.5, 1.0, and 1.5 are a result of the Rossiter-McLaughlin effect (Rossiter 1924; McLaughlin 1924)

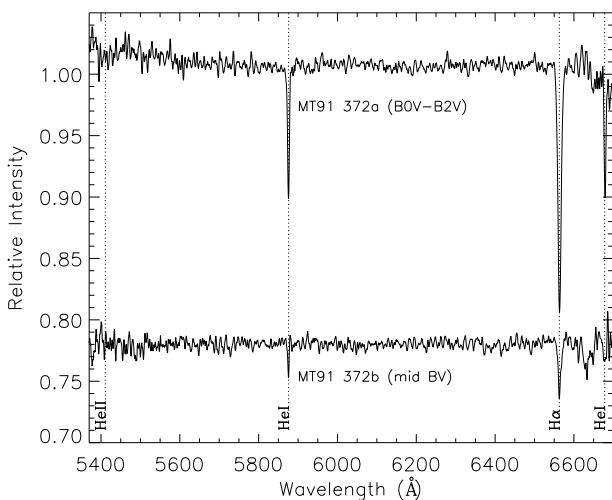


FIG. 5.— Normalized component spectra for MT91 372a and MT91 372b using the González & Levato (2006) technique for disentanglement. The spectra are shown with arbitrary vertical offsets.

two strong signals, the likely period at ~ 2.218 d and the $1-\nu$ alias at ~ 1.821 d. The BSCSP solution also converged on a 2.218 d period.

Our photometric and spectroscopic data, adopted T_1 , and starting orbital parameter guesses were used to compute the best-fit PHOEBE orbital solution displayed in Figure 4. The best period for the combined datasets is $P = 2.227490 \pm 0.000005$ days, and the light curve requires a non-zero, but low, eccentricity of $e = 0.044 \pm 0.002$. The best PHOEBE solution provides a slightly lower mass ratio of $q = 0.44 \pm 0.01$ (BSCSP yields $q = 0.50 \pm 0.02$). Table 2 lists the best-fit orbital parameters, including the orbital period (P), the date of periastron (T_0), eccentricity (e), orbital inclination (i), semi-major axis (a), systemic velocity (γ), and mass ratio (q). Table 2 also lists physical parameters for the system derived from the modeling process, including the secondary temperature (T_2), the radii of both components (R_1 and R_2), the masses (M_1 and M_2), and the bolometric magnitudes (M_{Bol1} and M_{Bol2}). Not surprisingly, given the depth of the eclipses, MT91 372 is nearly edge-on with an inclination of $i = 86 \pm 1^\circ$. This results in computed component masses of $13.0 \pm 0.7 M_\odot$ and $5.7 \pm 0.4 M_\odot$ and radii of $4.94 \pm 0.04 R_\odot$ and $3.34 \pm 0.06 R_\odot$. Coupled with the estimated primary temperature and the resulting best fit secondary temperature ($T_2 = 16,600 \pm 2,300$), the best-fit spectral types are B1V and B5V (Drilling & Landolt 2000), agreeing well with our initial estimates. The final rows of Table 2 list the adopted extinction ($A_V = 7.07 \pm 0.12$), and the observed out-of-eclipse apparent magnitude of the system ($m_V = 14.96$), the distance modulus (D.M.), and the resulting distance (d) in kpc. Given the derived bolometric magnitudes (-4.87 mag and -2.41 mag for the primary and secondary, respectively), the distance modulus may be computed in the standard manner,

$$\begin{aligned} D.M. &= m_V - M_V - A_V \\ &= m_V + 2.5 \log(10^{-(M_{Bol1}-BC_1)/2.5}) \\ &\quad + 10^{-(M_{Bol2}-BC_2)/2.5} - A_V. \end{aligned} \quad (1)$$

The resulting distance modulus of 10.62 ± 0.28 equates to a distance of 1.33 ± 0.17 kpc. We note here that the uncertainties on M_{Bol1} and M_{Bol2} are coupled, not independent, since T_2 is derived from T_1 via the ratio of eclipse depths. Furthermore, there is an anti-correlation between bolometric magnitudes (i.e., temperatures) and the bolometric corrections (B.C.), meaning that an error in M_{Bol} is partially canceled by a change in B.C. in the opposite direction. Consequently, the derived M_V used to determine the distance modulus is less sensitive than one might ordinarily assume to the adopted primary effective temperature, T_1 . Nevertheless, the relatively large uncertainty on the temperature of MT91 372A is the dominant source of uncertainty on the derived distance for this system.

4.4. MT91 696

When corrected for third light contributions, MT91 696 is also a good object for determining the distance to Cyg OB2. As a relatively bright ($m_V = 12.05$ mag), short-period system ($P = 1.46918$ d), it contains components close in spectral type (O9.5V and B0.5V) and

luminosity (Kiminki et al. 2012), the system is nearly edge-on with eclipse depths of ~ 0.64 mag. Figure 6 displays the radial velocity curves (top), light curve (middle), and light curve residuals (bottom). The solid curves represent the best-fit PHOEBE model discussed below. The smooth, continuous variation in the light curve indicates that the components are near contact. Velocity and photometric uncertainties are small compared to the variations.

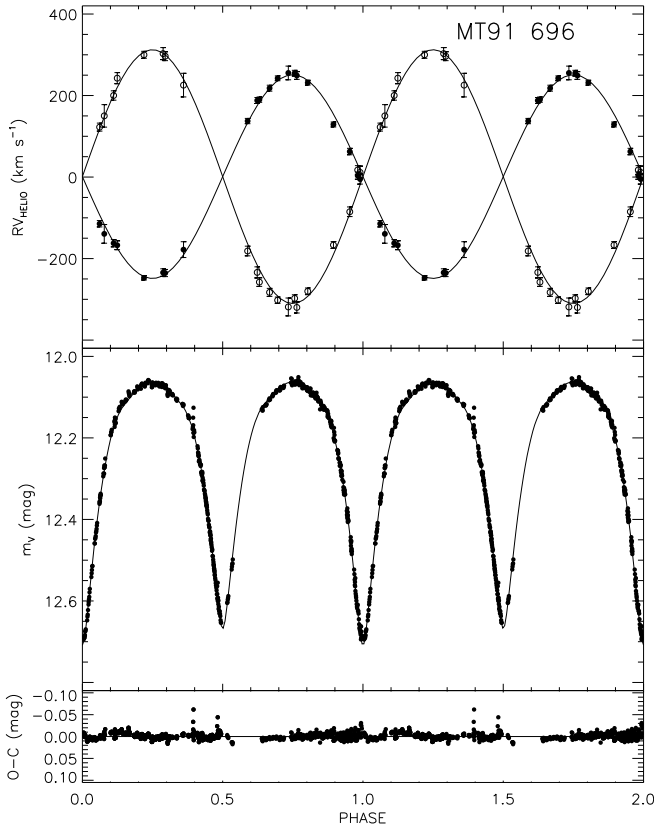


FIG. 6.— Radial velocity curve (top), light curve (middle), and light curve residuals (bottom) for MT91 696. Solid and unfilled points (top) denote the primary and secondary radial velocities, respectively. Solid curves in each panel show the best-fit PHOEBE solutions given the adopted parameters, as described in the text.

To estimate the component temperatures, we utilized 21 epochs of WIRO-Longslit spectra taken over nine nights between 2008 August 20 and 2012 October 21 to disentangle the component spectra (shown in Figure 7) and obtain the cross-correlation radial velocities listed in Table A.1. In the disentangled primary spectrum, the EW ratio of temperature-sensitive lines EW_{5411}/EW_{5876} is 0.45 ± 0.05 . We estimate the ratio for the secondary to be $EW_{5411}/EW_{5876} = 0.25 \pm 0.05$. We also measured the equivalent width ratio using a composite of four spectra obtained near a single quadrature phase ($\phi = 0.75$). The measured ratios were higher using this method, 0.76 ± 0.07 and 0.53 ± 0.07 for the primary and secondary respectively. We adopted the mean of these ratios, 0.61 ± 0.09 for the primary and 0.44 ± 0.09 for secondary. Using the relationship shown in Figure 3, this yields $T_1 = 32,000 \pm 600$ K and $T_2 = 29,800 \pm 700$ K. The primary temperature is similar to the 31,884 K im-

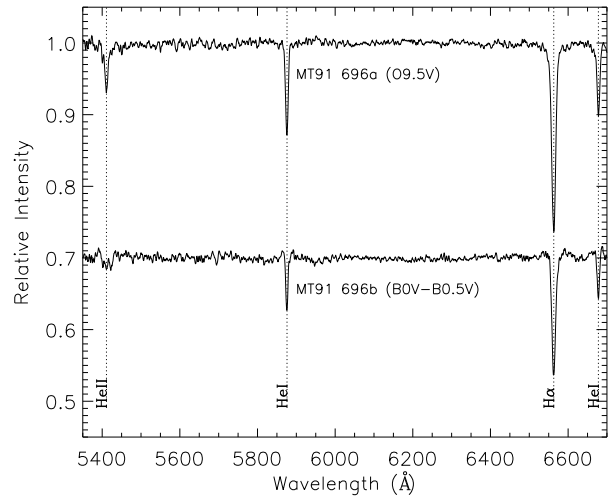


FIG. 7.— Normalized component spectra for MT91 696A and MT91 696B using the González & Levato (2006) technique for disentanglement. The secondary spectrum is shown with an arbitrary vertical offset for clarity.

plied by the observational scale of Martins et al. (2005) for an O9.5V. Accordingly, we adopt $T_1 = 32,000 \pm 600$ as a fixed parameter in the PHOEBE modeling but leave T_2 as a free parameter to be fit.

Before considering the third light contribution from MT91 696C, we computed the best-fit PHOEBE model to the photometry that includes this extra component. We then tested various orbital configurations, and each indicated that the system is just barely detached. Once the code converged on the best-fit solution, we added increasingly larger contributions from third light until PHOEBE could no longer converge on a solution and the primary eclipse depth exceeded 0.75 magnitudes. The highest contribution allowed was 14% of maximum out-of-eclipse light (i.e., 14% of the $V=12.051$ mag system). This indicates that the tertiary cannot be brighter than about $V=14.18$ mag. Our ephemeris indicates that the *HST* FGS measurement was taken at a phase near maximum light. The 0.94 ± 0.40 mag offset between the (A+B) binary and the brightest astrometric companion, as reported by Caballero-Nieves et al. (2014), results in a nominal contribution of $22^{+20\%}_{-12\%}$ — consistent with the maximum of 14% allowed by the light curve. We therefore adopt a contribution of 14% for component c.

Table 2 displays the resulting system parameters for the best solution to the MT91 696 system after including a constant 14% third light contribution within the PHOEBE model and fixed zero eccentricity (when allowing the eccentricity to vary, BSCSP and PHOEBE both converged on the same zero eccentricity solution). The final orbital period obtained with all radial velocity and light curve information is in excellent agreement with the period reported by Souza et al. (2014), indicating there has been negligible change in the period over six years. Additionally, while the computed radii ($R_1 = 6.36 \pm 0.03 R_\odot$ and $R_2 = 5.72 \pm 0.02 R_\odot$) are slightly smaller than the theoretical values of $7.3 \pm 0.1 R_\odot$ (O9.5V) and $6.6 \pm 0.1 R_\odot$ (B0.5V), the computed masses ($M_1 = 15.0 \pm 0.2 M_\odot$ and $M_2 = 12.1 \pm 0.8 M_\odot$) are in good agreement with the the-

TABLE 2
JOINT LIGHT AND VELOCITY CURVE ANALYSIS FOR MT91 372, MT91 696, CPR2002 A36, AND SCHULTE 3

	MT91 372	MT91 696	CPR2002 A36	Schulte 3
P (days)	2.227582 ± 0.000005	1.469179 ± 0.000001	4.6749 ± 0.0006	4.74591 ± 0.00005
T_O (HJD-2,400,000)	56100.854 ± 0.001	54731.6401 ± 0.0005	55725.8 ± 0.2	53996.093 ± 0.006
e	0.044 ± 0.002	0 (fixed)	0 (fixed)	0 (fixed)
A (R_\odot)	19.0 ± 0.3	16.3 ± 0.2	38.7 ± 0.8	36.0 ± 0.9
q	0.44 ± 0.01	0.80 ± 0.02	0.62 ± 0.02	0.42 ± 0.03
V_O (km s^{-1})	-7 ± 2	1.1 ± 2.7	-29 ± 3	-47 ± 3
i (degrees)	86 ± 1	86.5 ± 1.5	73 ± 1	59.2 ± 0.3
3rd light	...	14% (fixed)	...	12% (fixed)
$\log(g)$ (P)	4.2	4.0	3.4	3.3
$\log(g)$ (S)	4.1	4.0	3.4	3.3
T_1 (K)	$24,000 \pm 3,000$	$32,000 \pm 600$	$30,000 \pm 2,000$	38,500
T_2 (K)	$16,600 \pm 2,300$	$30,940 \pm 1,050$	$20,600 \pm 600$	$31,300 \pm 700$
R_1 (R_\odot)	4.94 ± 0.04	6.36 ± 0.03	16.4 ± 0.1	16.5 ± 0.1
R_2 (R_\odot)	3.34 ± 0.06	5.72 ± 0.02	13.1 ± 0.1	11.0 ± 0.1
M_1 (M_\odot)	13.0 ± 0.7	15.0 ± 0.2	22 ± 2	20 ± 2
M_2 (M_\odot)	5.7 ± 0.4	12.1 ± 0.8	14 ± 1	8.2 ± 0.9
Spectral Type 1	B1V	O9.5V	O9 – O9.5III:	O6V
Spectral Type 2	B5V	B0.5V	O9.5 – B0IV:	O9III – O9II
M_{Bol1} (mag)	-4.87 ± 0.60	-6.66 ± 0.14	-8.44 ± 0.30	-9.54 ± 0.54
M_{Bol2} (mag)	-2.41 ± 0.68	-6.29 ± 0.20	-6.32 ± 0.30	-7.76 ± 0.39
$B.C._1$ (mag)	-2.38 ± 0.33	-3.05 ± 0.09	-2.88 ± 0.16	-3.59 ± 0.37
$B.C._2$ (mag)	-1.45 ± 0.38	-2.96 ± 0.10	-2.01 ± 0.17	-2.99 ± 0.15
$M_{V,1}$ (mag)	-2.49 ± 0.27	-3.61 ± 0.04	-5.56 ± 0.15	-5.95 ± 0.17
$M_{V,2}$ (mag)	-0.96 ± 0.30	-3.33 ± 0.10	-4.32 ± 0.13	-4.77 ± 0.25
M_V (mag)	-2.73 ± 0.28	-4.24 ± 0.07	-5.86 ± 0.14	-6.26 ± 0.19
A_V (mag)	7.07 ± 0.12	5.85 ± 0.09	6.46 ± 0.23	6.02 ± 0.09
m_V (mag)	14.96 ± 0.02	12.22 ± 0.01^a	11.40 ± 0.01^b	$10.36 \pm 0.03^{a,b}$
RMS_V (mag)	0.023	0.007	0.015	0.013
RMS_{NSVS} (mag)	0.035	0.043
RMS_{RV1} (km s^{-1})	10.2	12.9	25.2	32.9
RMS_{RV2} (km s^{-1})	14.3	19.3	20.5	37.6
D.M. (mag)	10.62 ± 0.28	10.61 ± 0.10	10.80 ± 0.27	10.60 ± 0.21
Dist. (kpc)	1.33 ± 0.17	1.32 ± 0.07	1.44 ± 0.18	1.32 ± 0.13

^a component A+B only

^b spot contribution removed

oretical values of $16.0 \pm 0.5 M_\odot$ and $12.9 \pm 0.4 M_\odot$ (Martins et al. 2005). Finally, the resulting secondary temperature, $T_2 = 30,940 \pm 1050$ K also agrees well with the direct T_2 measurement from the He II $\lambda 5411/\text{He I } \lambda 5876$ line ratio determined above.

The light curve residuals in the lower panel of Figure 6 show small $<1\%$ systematic variations between phase 0 and 0.25, suggesting minor deficiencies in the adopted model, but additional high-quality photometry will be needed to further constrain the model parameters. The computed distance modulus is 10.61 ± 0.10 mag and corresponds to a distance of $d=1.32 \pm 0.07$ kpc. For this system, the largest source of uncertainty on the distance is the uncertainty on the correction for interstellar extinction.

4.5. CPR2002 A36

Ideally, eclipsing binary distances would make use of detached systems which have simple geometries, i.e., the stars are spherical and the light curves are unaffected by complications involving mass loss, hot spots produced by radiation or mass transfer streams, and variations in the surface potentials of stars approaching or undergoing Roche lobe overflow. Unfortunately, four of the six known eclipsing SB2 systems in the direction of Cyg OB2 contain evolved components and are probable contact or over-contact systems. Therefore, we proceed to model

the CPR2002 A36 and Schulte 3 eclipsing SB2 systems while cautioning that the interpretation of the velocity curves and light curves is subject to larger uncertainties.

Figure 8 shows the best-fit light curve data and model (top), velocity curve data and model (middle), and light curve residuals (bottom) for CPR2002 A36. The light curve is characteristic of an over-contact system with a difference in eclipse depths that indicates a significant difference in component effective temperatures. Additionally, we see an O’Connell effect that results in an ~ 0.04 mag difference in maxima. There is also considerable dispersion in the $NSVS$ magnitude at nearly all phases, exceeding the nominal 0.01 mag uncertainties and suggestive of a high level of intrinsic temporal variability. Finally, because of the over-contact nature of the system, CPR2002 A36 shows strong, varying $H\alpha$ emission and a Struve-Sahade effect in the He I lines.

The emission and Struve-Sahade effect are mostly responsible for the disagreement between the observed and calculated radial velocities. Emission partially fills the spectral lines and skews the He I line centers and is most significant for phases $\sim 0.8 - 1.1$ when the secondary is heading into eclipse. This emission is easiest to see at $H\alpha$, shown in the panel second from right in Figure 9 (colored white in this inverse greyscale image), a phased spectral sequence using all of the WIRO-Longslit spectra folded with the final solution period. The figure also shows

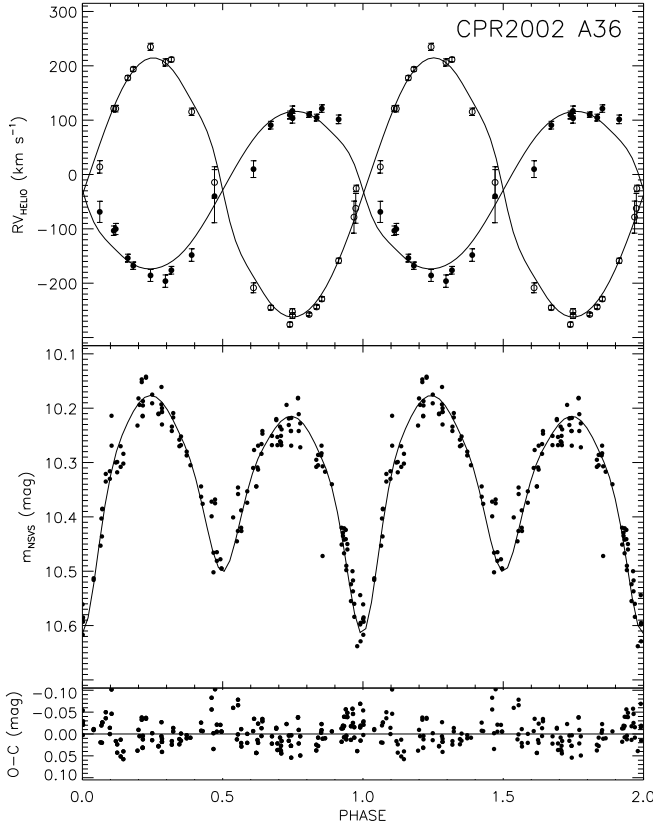


FIG. 8.— Radial velocity curve (top), light curve (middle), and light curve residuals (bottom) for CPR2002 A36. Solid and unfilled points (top) denote the primary and secondary radial velocities, respectively. Solid curves in each panel show the best-fit PHOEBE solutions given the adopted parameters, as described in the text.

four additional spectral lines in the $\lambda\lambda 5400 - 5700 \text{ \AA}$ range: He II $\lambda 5411$, O III $\lambda 5592$, He I $\lambda 5876$, and H α , and He I $\lambda 6678$. The orange and green curves represent the final primary and secondary solutions, respectively. From a phase of $\sim 0.25 - 0.6$, a singular emission feature is evident and appears to be associated with the redshifted secondary. At phase $0.85 - 1.1$, there appear to be multiple emission components with the dominant one still associated with the secondary. At He I $\lambda 5876$ (middle panel), the emission results in the best Gaussian fit being centered at a longer wavelength than the true center. Because the primary component's He I absorption is weaker and shifted less, the He I profiles are more distorted at these phases, and therefore, computed radial velocities are more skewed. The emission, Struve-Sahade effect, and O'Connell effect may be adequately explained by a hot spot or a stream of optically thin ionized gas near or trailing the secondary.

An advantage to creating a phased spectral image is that weak lines that would normally be difficult to identify amongst the continuum noise and various interstellar/DIB lines are more easily identified and associated with the correct component. For instance, O III $\lambda 5592$ is difficult to identify with certainty in many of CPR2002 A36's spectra, but its presence is easily revealed in both components in Figure 9. The full phased spectral image also reveals moderately weak C IV $\lambda\lambda 5801, 5812$ absorption and very weak C III $\lambda 5696$

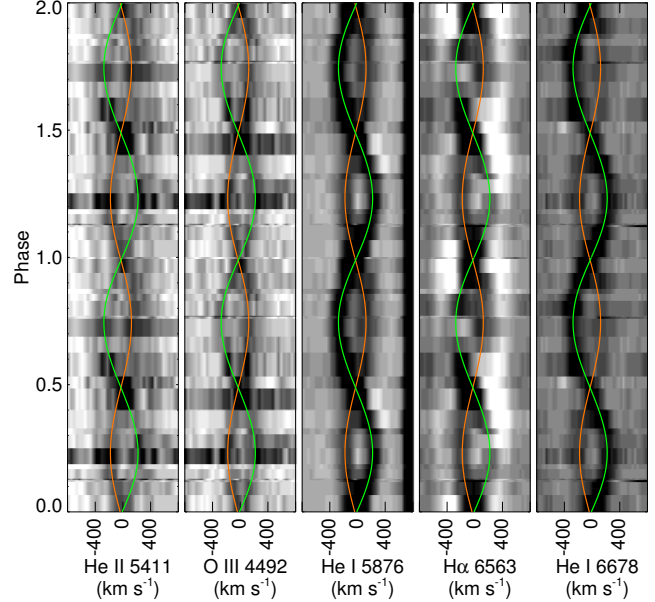


FIG. 9.— A sequence of spectra for CPR2002 A36 ordered by orbital phase, showing five spectral lines with the spectroscopic orbital solution overplotted in orange for the primary and green for the secondary.

emission in the primary, the presence and strength of which, with He II $\lambda 5411$, indicate the primary may be slightly hotter than the B0 estimated in Kiminki et al. (2009), such as O9 – O9.5 (Walborn 1980). Given the strength of the metal lines in these spectra and of the Si IV and C III lines shown in Figure 4 of Kiminki et al. (2009), we revise our estimate of the primary's luminosity class to III and adopt a full spectral classification of O9 – O9.5III. For the secondary, the full phased spectral image revealed the presence of weak N II $\lambda\lambda 5667, 5670, 5680$. Given these, the weak He II $\lambda 5411$, and the very weak O III $\lambda 5592$, we revise and adopt the spectral type of O9.5 – B0IV: for the secondary.

We estimate the effective temperatures for this system in a similar manner to MT91 696 via the ratio of helium equivalent widths. We measured equivalent widths at both quadrature phases, obtaining $EW_{5411}/EW_{5876} = 0.52 \pm 0.09$ and $EW_{5411}/EW_{5876} = 0.48 \pm 0.04$ for the primary and secondary, respectively. As both components of CPR2002 A36 have been classified as likely evolved, we use the dashed line in Figure 3 to estimate the temperatures as $T_1 = 29,400 \text{ K}$ and $T_2 = 29,200 \text{ K}$ with uncertainties of approximately 500 K. These estimates are in rough agreement with the theoretical temperatures for an O9III ($31,000 \pm 800 \text{ K}$) and O9.5IV ($30,800 \pm 500 \text{ K}$), but disagree with the temperature difference indicated by the difference in eclipse depths. However, considering the lower signal-to-noise of He II $\lambda 5411$ in many of the spectra and the fact that the Struve-Sahade effect raises the inherent uncertainty in equivalent width measurements of He I, and given the theoretical temperatures (Martins et al. 2005) for the estimated spectral types above, we adopt $30,000 \pm 2,000 \text{ K}$ for T_1 and estimate $29,000 \pm 2,000 \text{ K}$ for T_2 .

Our nominal PHOEBE model is a double-contact configuration with a hot spot on the trailing side of the secondary (130° from the point of contact on the equa-

tor). In this scenario, the visibility of the spot coincides well with the presence of emission in Figure 9. The spot may indicate the transfer of mass from the primary. The final solution is fit with a spectroscopic period of $P = 4.6749 \pm 0.0006$ d and eccentricity fixed at zero. We were unable to reconcile a phase shift of 0.157 (17.6 hr) between the NSVS photometry and our radial velocity data with PHOEBE. Therefore, we adopted the ephemeris obtained from BSCSP and applied an arbitrary 0.1565 phase shift to the NSVS photometric data. Similarly, we applied an arbitrary 0.0506 phase shift to the RBO V-band photometry as well. It is possible that the system has a changing period that we have not accounted for, but its impact is negligible on the results presented here. Additionally, we find that the V-band photometry and the radial velocity curves are better fit with a slightly higher inclination than the NSVS photometry ($i = 72.9^\circ$ versus $i = 69.6^\circ$). Because NSVS photometry is filterless and only approximate to Johnson-R band (Woźniak et al. 2004), we adopt the solution with the higher inclination. This also has negligible impact on the results presented here. In Figure 8, we show the NSVS photometry instead of the V-band photometry because its full phase coverage better illustrates the solution's overall agreement with the observed light curves.

The final solution yields a secondary temperature of $T_2=20,600 \pm 600$ K, contrasting significantly with the $29,000 \pm 2,000$ K estimated by helium equivalent width ratios, but relative to T_1 , it is in better agreement with the temperature difference indicated from the eclipse depths. No combination of spot parameters and overall model allowed for a higher secondary temperature, but we admit that fitting the spot manually limits the parameter space explored. The computed masses $M_1=22 \pm 2 M_\odot$ and $M_2=14 \pm 1 M_\odot$ are in good agreement with the expected values from Martins et al. (2005). However, the radii, $R_1=16.4 \pm 0.1 R_\odot$ and $R_2=13.1 \pm 0.1 R_\odot$, are larger than the expected values and more characteristic of O9II and O9.5III. However, given the uncertainties on the spectral types, and the fact that each component is filling its Roche lobe, these values are not entirely surprising. Using the computed bolometric magnitudes in Table 2, we compute a distance for this system of 1.44 ± 0.18 kpc, where the uncertainty on distance is dominated by the relatively large uncertainty on interstellar extinction ($\sigma_{A_V}=0.23$ mag) and the uncertainty on primary temperature ($\sigma_T=2000$ K). Had we adopted the CCM89 reddening law for CPR A36 instead of FM07, the resulting distance would drop to 1.27 kpc.

4.6. Schulte 3

Schulte 3 shows many similarities to CPR2002 A36, including highly variable H α emission, a Struve-Sahade effect, an O'Connell effect, and a similar period (4.74591 ± 0.00005 d). Figure 10 shows the velocity curve data and model (top), light curve data and model (middle), and the light curve residuals (bottom). In the top panel, squares represent WIRO data, triangles represent WIYN data, and stars represent WIRO data excluded when determining the BSCSP and PHOEBE solutions. We excluded these data because of the distortion of the He I $\lambda 5876$ profiles near quadrature. Like CPR2002 A36, this distortion, the Struve-Sahade effect, more strongly affects the primary radial velocities and is more easily seen in

H α , shown in the bottom panels of Figure 11 (colored white in this inverse greyscale image). The figure is a phased spectral sequence using all of the Hydra and WIRO-Longslit spectra folded with the final solution period, where the orange and green lines represent the primary and secondary spectroscopic solutions plotted over various spectral lines, respectively. The emission in H α and He I appears at slightly different phases than with CPR2002-A36, indicating a different spot geometry and location. In the Figure, H α shows a singular emission feature, which appears to be associated with the redshifted secondary, at phases $\sim 0.25 - 0.5$. At phases $0.6 - 1.0$, it shows multiple emission components with the dominant one still associated with the secondary. This emission is also present in He I $\lambda 5876$, but it is more difficult to see in the Figure owing to its weaker presence in the wings around this line. Regardless, the primary component's He I radial velocities are skewed at these phases for the same reasons given for CPR2002 A36. We obtained 20 epochs of WIYN/Hydra spectra and 24 epochs of WIRO-Longslit spectra. Radial velocities were measured for 12 and 19 of these spectra, respectively. However, because of the distorted line profiles we utilized only WIYN radial velocities for the primary and excluded all secondary He I $\lambda 5876$ radial velocities near $\phi = 0.25$. The quality of the final solution is demonstrated with the good agreement between the radial velocity curves and the spectroscopic solutions in Figure 11. In addition to H α in the bottom-right panel, the top-right panel shows Si IV 4089 Å, N III 4097 Å, H δ 4101 Å, and Si IV 4116 Å, and the middle right panel shows He I 5876 Å. We provide all radial velocities in Table A.1, with a note to designate the observations excluded from fitting. The table also includes the observed minus calculated values of the excluded points for reference.

We also utilized the WIYN spectra, after removing contributions from interstellar Ca II and the diffuse interstellar band (DIB) at $\lambda 4428$ Å, to disentangle the component spectra. Because the variability of the He I line depths more strongly affects the primary than the secondary, He I is underrepresented in the disentangled primary spectrum. The spectrum shows $EW_{4200}/EW_{4026} > 1$, indicating a temperature class of early to mid-O. However, taking into account that He I is underrepresented, the ratio may be closer to unity, indicating a temperature class near O6 – O7. Additionally, the weak N III with absent O II, N II, and Si IV, indicates a likely luminosity class of V. The disentangled secondary spectrum shows EW_{4200}/EW_{4144} near unity, indicating a temperature class near O9, and the strength of Si IV and N III lines relative to the neighboring He I lines indicates an evolved luminosity class, likely III – II. The disentangled component spectra are shown at top and third from top in Figure 12. The spectra show good agreement with the spectral standards of HD101190 (O6V; second from top) and HD148546 (O9Ia; bottom) from the Walborn & Fitzpatrick (1990) digital atlas. We note that HD101190 has a luminosity of Ia rather than III, resulting in stronger metal lines, but it is the closest standard in the library. Interestingly, the secondary luminosity class suggests that the present secondary may have been the more massive component at one point.

As with the other systems, we measured the effective

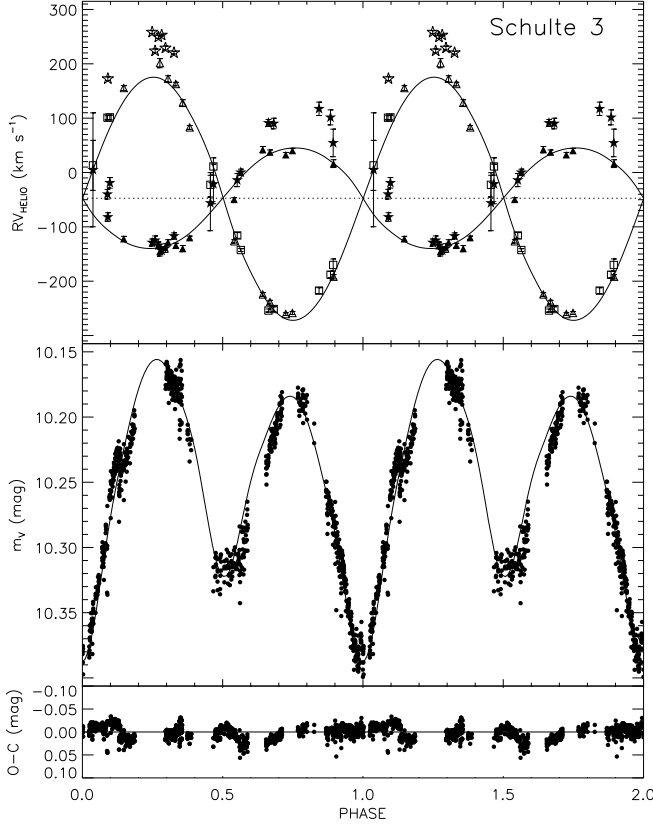


FIG. 10.— Radial velocity curve (top), light curve (middle), and light curve residuals (bottom) for Schulte 3. Solid and unfilled points (top) denote the primary and secondary radial velocities, respectively. Squares represent observations with WIRO-Longslit, triangles represent observations taken with WIYN-Hydra, and stars represent the observations excluded from fitting. Solid curves in each panel show the best-fit PHOEBE solutions given the adopted parameters, as described in the text.

temperatures using the ratio of helium line equivalent widths in spectra obtained near quadrature. We find that EW_{5411}/EW_{5876} is 1.06 ± 0.06 for the primary and 0.95 ± 0.04 for the secondary. Here, the Struve-Sahade effect either does not impact our equivalent width measurements or it impacts them equally, as the variation in He I line profile associated with the primary appears to be limited to line depth and width changes only; the overall equivalent width does not change between quadrature phases. With these equivalent width ratios and the luminosity class estimates, the relations provided in Figure 3 yield temperatures of $T_1 = 34,500 \pm 500$ K and $T_2 = 32,000 \pm 500$ K for the primary and secondary, respectively. The secondary estimate is nearly in agreement with the theoretical value of $31,300 \pm 600$ K from Martins et al. (2005). However, the primary estimate is lower than the theoretical value for an O6V by approximately 4,000 K, which makes the temperature more appropriate for a slightly later type of O7 (Martins et al. 2005). Given that we cannot fully quantify the effect that emission plays with the equivalent width ratios, we also consider that the effective temperature may be as high as 38,500 K for the primary. Therefore, we computed a grid of solutions for primary temperatures 34,000 K – 38,500 K. In these solutions, the secondary temperatures from $\sim 28,000$ K – 35,500 K depending on spot parame-

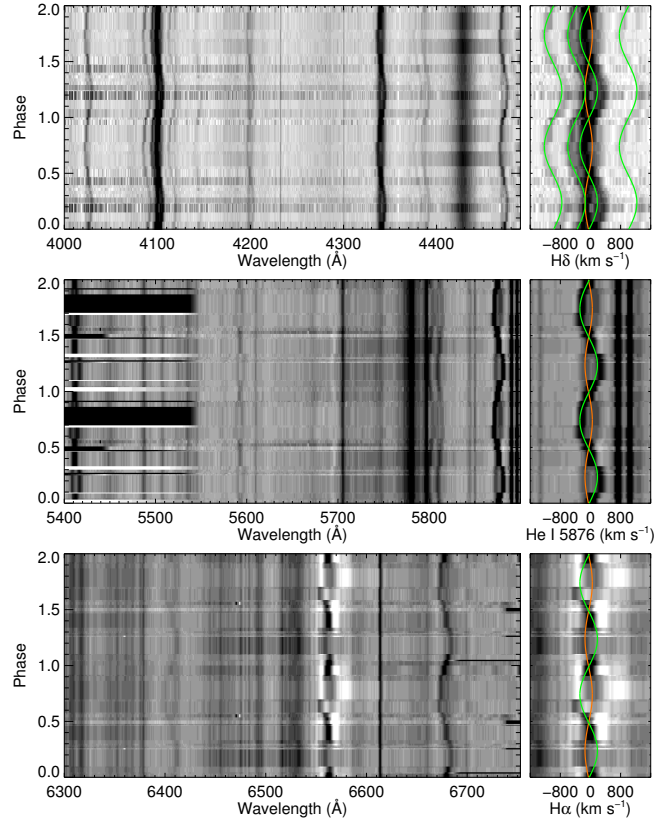


FIG. 11.— A sequence of spectra for Schulte 3 ordered by orbital phase, showing nearly the entire wavelength range covered by our WIYN and WIRO observations. Right panels illustrate the quality of the overall solution with spectroscopic orbital solution overplotted in orange for the primary and green for the secondary.

ters and model used.

The light curve for Schulte 3 is unambiguously characteristic of a contact/overcontact system. It exhibits relatively small eclipse depths of ~ 0.23 mag and ~ 0.17 mag in the raw light curve, suggesting a moderate inclination. Similarly to CPR2002 A36, the light curve also displays an O'Connell effect (~ 0.02 – 0.03 mag) with a brighter primary maximum and exhibits real photometric variability in excess of the nominal uncertainties. Photometry obtained at similar orbital phase across different orbits exhibit offsets of up to 0.02 mag, signifying intrinsic variability. This is probably a triple system, and therefore the light curve (and to some minor extent, the velocity curves) is further complicated by the presence of Schulte 3C which contributes $\simeq 12\%$ to the V-band light. We used PHOEBE to account for the third light contribution.

We explored various combinations of temperatures for the primary, secondary, and spot, various spot configurations, and both W-Uma and double-contact configuration models for Schulte 3. Because the emission features appear to be associated mainly with the secondary, we placed the relatively large (49 – 60°) hot spot on that component, with a center between 24° and 45° from the northern pole and between 20° and 35° counter-clockwise from the point of contact. The adopted location of this hotspot coincides well with the presence of emission seen in H α . In the end, we adopted the solution

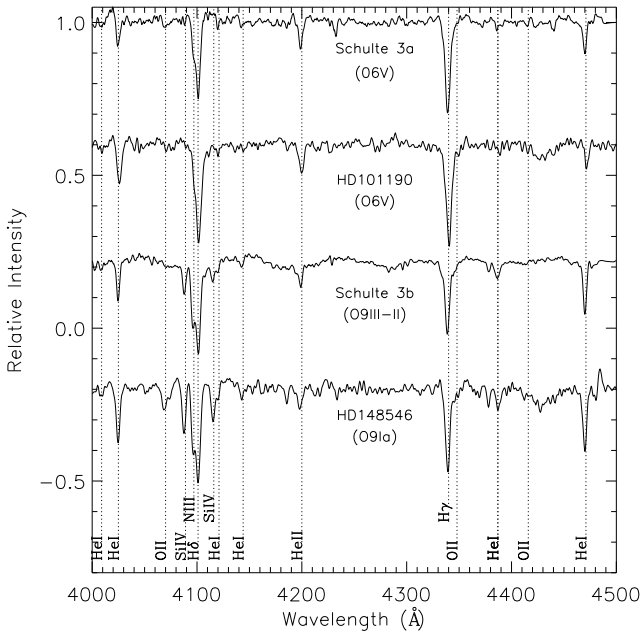


FIG. 12.— Normalized component spectra for Schulte 3A and Schulte 3B using the [González & Levato \(2006\)](#) technique for disentanglement. Comparison standard spectra from the atlas of [Jacoby et al. \(1984\)](#) appear below each component spectrum. The spectra are shown with arbitrary vertical offsets.

with $T_1 = 38,500$ K and $T_2 = 31,300$ K from [Martins et al. \(2005\)](#) because our confidence in the spectral types exceeded that of the compromised equivalent width ratios. Additionally, the spot placement for this solution is nearer to the point of contact (45° from the northern pole and centered 35° in the direction of rotation) than the other models, which makes sense if the primary is heating the secondary. This solution also provides the most consistent overall picture. The spot is similar in temperature to the primary ($T_{spot} = 37,560$ K), just as we would expect if it originates from heating, and both the secondary and combined secondary+spot temperatures ($T_{2+spot} = 32,615$ K) agree with the value obtained from the less compromised secondary equivalent width ratios. Finally, the combined secondary+spot and primary temperatures are in better agreement with the temperature difference implied by the light curves. This solution yields a distance of 1.32 kpc.

However, if we accept the temperatures estimated strictly from equivalent widths, (i.e., $T_1 = 34,500$ K and $T_2 = 32,100$ K), then our best fit is a double contact configuration with a spot inclined $\sim 23^\circ$ from the northern pole, centered $\sim 20^\circ$ in the direction of rotation from the point of contact, and with a radius of $\sim 49^\circ$. The average secondary+spot temperature is $\sim 34,800$ K. This does not agree with the significant difference in component temperatures suggested by the light curve. Additionally, the spot temperature required with this geometry is nearly 45,000 K, which may be possible with a mass stream origin but not heating. The computed distance for this scenario is 1.27 kpc.

The computed distance to all explored configurations was between 1.21 kpc and 1.36 kpc, with the closest distance resulting from a solution with $T_1 = 34,000$ K,

$T_2 = 28,596$ K, and $T_{spot} = 34,315$ K. In all solutions, most light-curve-derived orbital parameters had little variation (e.g., $i \simeq 59^\circ$, $R_1 \simeq 16.5 R_\odot$, and $R_2 \simeq 11 R_\odot$). The largest source of variation/uncertainty originates from the temperatures and resultant bolometric magnitudes, with the second largest source being the high uncertainty in interstellar reddening. Because of the degeneracies present in this system, when computing uncertainties, we folded in the full variation of all values for all explored configurations. We provide these with the full list of orbital parameters in Table 2 and adopt a distance of 1.32 ± 0.13 kpc to Schulte 3. Additionally, the light curve residuals are systematic beyond the stated uncertainties, indicating additional physical effects that are not correctly reproduced in any of the explored models.

5. DISCUSSION

The weighted mean distance of the four eclipsing binaries analyzed here is 1.33 ± 0.06 kpc. The unweighted mean distance is 1.35 kpc. This value is broadly consistent with the 1.3 – 1.5 kpc distances measured for radio masers in pre-main-sequence objects in the surrounding molecular clouds ([Rygl et al. 2012](#)). It is also in good agreement with the [Dzib et al. \(2012\)](#) estimate of 1.3 – 1.4 kpc toward the massive binary Schulte 5. However, our mean distance is somewhat smaller than many measurements in the literature which lie in the range 1.4 – 1.7 kpc. In particular, [Hanson \(2003\)](#) obtained a spectrophotometric distance of 1.45 kpc toward an ensemble of Cyg OB2 stars. Interestingly, [Hanson \(2003\)](#) noted that had she adopted the (at that time, newly revised) cooler stellar effective temperature scale of [Martins et al. \(2002, 2005\)](#) this would place Cyg OB2 at 1.2 kpc (D.M.=10.44). She rejected this possibility, concluding that such a small distance would reduce the luminosity of Cyg OB2 O supergiants that have known mass loss rates and create a problem for the theoretical understanding of the mechanisms that drive massive star winds. However, given recent downward revisions of the stellar mass loss rates ([Puls et al. 2008](#)) it is no longer clear that this is a compelling reason for rejecting a smaller distance. If we were to adopt the [Hanson \(2003\)](#) distance of 1.20 kpc and correct it upward by a factor of 1.08 to account for the additional luminosity of secondary stars in close massive systems as recommended by [Kiminki & Kobulnicky \(2012\)](#), the resulting distance is 1.30 kpc, in excellent agreement with our current eclipsing binary estimate.

We note here that [Wright et al. \(2015\)](#) derived slightly lower extinctions of $A_V = 6.98^{+0.50}_{-0.26}$ mag and $5.81^{+0.32}_{-0.29}$ mag for MT91 372 and MT91 696, respectively, by using a different set of UV photometry. If we had adopted these extinctions, it would have increased the resulting distances to these systems to 1.39 and 1.34 kpc, respectively. The overall weighted mean distance would have risen slightly to 1.36 ± 0.10 kpc. This small systematic difference is within the uncertainty of our measurement, but it underscores the sensitivity of the distance measurement to the adopted correction for interstellar extinction.

The level of agreement between our four distance measurements is remarkable given the stated (perhaps overly generous) uncertainties stemming primarily from uncertainties on effective temperatures and interstellar reddening.

ings. We regard this to be a coincidence given that the analysis of each system has entailed independent measurements of these key observable quantities arising from independent datasets. The adopted photometry, reddnings, and stellar effective temperatures are independently justified in each case, and we do not believe that an artificial level of agreement has been imposed during the analysis process.

Figure 13 displays a three-color representation of the Cyg OB2 vicinity, with blue, green, red depicting the *Spitzer Space Telescope* IRAC 4.5 μm , IRAC 8.0 μm , and MIPS 24 μm bands, respectively. Figure 13 shows the complex nature of this region, including stellar photospheres (blue), photo-dissociation regions at the edges of molecular clouds (diffuse green tracing broad emission features arising from excited polycyclic aromatic hydrocarbons, and hot dust (red). White circles indicate the 48 known binary systems in Cyg OB2 (Kobulnicky et al. 2014), while magenta labels highlight the known eclipsing binary systems and their distances. The yellow scale bar indicates the linear extent of 10 pc at 1.33 kpc distance. Blue labels mark four masers having radio parallax distances (Rygl et al. 2012) and the massive eclipsing binary Schulte 5 (Dzib et al. 2012).

The maser distance measurements range from 1.3 – 1.5 kpc, in agreement with most of the eclipsing binaries. Given the large angular extent of the Cygnus X region (almost a degree!), the entire star-forming complex containing Cyg OB2 could reasonably stretch 100 pc or more along the line of sight, thereby encompassing the various massive young stellar objects with maser parallaxes. The eclipsing binary CPR2002 B17 has a rather uncertain distance at 1.5 – 1.8 kpc (Stroud et al. 2010) and could be part of an extended star-forming complex somewhat further away than Cyg OB2. Schulte 5 is something of an enigma. Both Linder et al. (2009) and Yaşarsoy & Yakut (2014) analyze the joint light-curve and velocity-curve solution to compute distances of 0.93 and 0.97 kpc, respectively. While they both present evidence for luminosity from a third body in this system, the magnitude of this contribution is not known. Nevertheless, a third or fourth body in the Schulte 5 system (Linder et al. 2009; Kennedy et al. 2010) would have to contribute nearly as much light as the two eclipsing components in order to raise the distance to the mean of other Cyg OB2 eclipsing systems. The radio parallax measurement of Schulte 5 by Dzib et al. (2012) yield 1.3 – 1.4 kpc, in good agreement with the other eclipsing binaries. Given that there is no known population of massive stars substantially in the foreground to Cyg OB2, we think it unlikely that Schulte 5 is a foreground object. Neither is it likely to be a runaway in the radial direction; its systemic velocity, reported as -55 km s^{-1} (Yaşarsoy & Yakut 2014), would allow it to travel <200 pc in the $\sim 3 - 4$ Myr lifetime of the most massive stars. A refined understanding of the components of Schulte 5 are likely to yield a larger distance in better agreement with the masers and eclipsing systems.

6. CONCLUSIONS

We have presented a photometric and spectroscopic analysis of four double-lined eclipsing binaries within the Cygnus OB2 Association. The joint analysis provides a measure of the temperatures, luminosities, and thereby, the distances to these systems. We find distances of 1.33 ± 0.17 , 1.32 ± 0.07 , 1.44 ± 0.18 , and 1.32 ± 0.13 kpc toward MT91 372, MT91 696, CPR2002 A36, and Schulte 3, respectively. We adopt a weighted mean of 1.33 ± 0.06 kpc as the best estimate for the distance to the Cygnus OB2 Association. These are the most direct distance estimates to this touchstone region of massive star formation, and they agree well with radio VLBI parallax measurements toward masers in the star-forming clouds on the periphery of Cyg OB2. Having a secure distance toward the stellar population of Cyg OB2 allows more certainty in the luminosities, mass loss rates, and other fundamental stellar quantities measured for the massive stars therein. Within several years we anticipate parallaxes from the *Gaia* space mission providing even more precise distances toward Cygnus X constituents. Although *Gaia*'s precision is likely to be limited in crowded regions near the Galactic Plane, refined post-mission analysis of the data may yield a parallax distance to a prominent region such as Cygnus OB2. It is our hope that this eclipsing binary distance may serve as a benchmark for such an attempt.

ACKNOWLEDGEMENTS

We would like to acknowledge the time, effort, and thoroughness of the anonymous referee in assisting us to make this a stronger manuscript. We thank Anirban Bhattacharjee for obtaining *V*-band images of Schulte 3 at WIRO. We are very appreciative that Saida Caballero-Nieves shared results from her adaptive optics imaging and *HST* Fine Guidance Sensor survey in advance of publication. REU summer students Eric Topel, Emily Rolen, and Katie Lester helped obtain photometry of MT91 372. Gregor Rauw encouraged us to pursue the eclipsing binary distances. Andrej Prša provided advice on the modeling of binary systems with *PHEobe*. Nick Wright provided helpful comments pertaining to the introduction and massive star population of Cyg OB2. WIRO staff James Weger and Jerry Bucher enabled this science through their efforts at the Observatory. Karen Kinemuchi contributed observing assistance and data analysis during an early phase of the Cyg OB2 program. We thank Robert D. Gehrz, John A. Hackwell, and the State of Wyoming for their vision in 1975 to build the Wyoming Infrared Observatory, without which this work would not have been possible. This work was supported by the National Science Foundation through Research Experience for Undergraduates (REU) program grant AST 03-53760, through grant AST 03-07778, and through grant AST 09-08239, and the support of the Wyoming NASA Space Grant Consortium through grant #NNX10A095H. D. Kiminki thanks the James Webb Space Telescope NIRCam project at the University of Arizona for salary support. *Facilities:* WIRO, RBO

REFERENCES

- Abbott, D. C., Biegling, J. H., & Churchwell, E. 1984, ApJ, 280, 671
 Baguñolo, W. G., Gies, D. R., Riddle, R., & Penny, L. R. 1999, ApJ, 527, 353

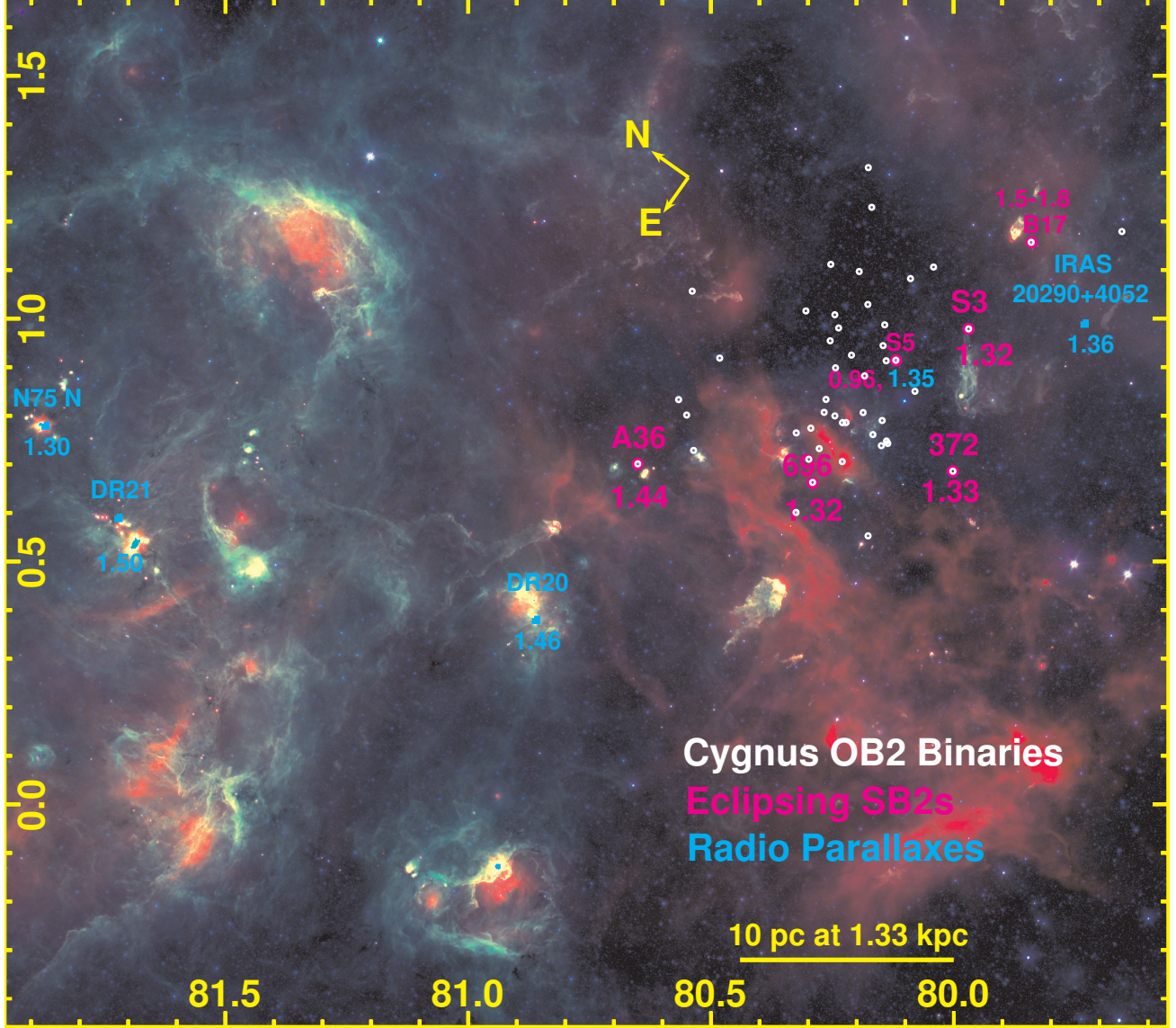


FIG. 13.— *Spitzer Space Telescope* 3.6 μm (cyan), 8.0 μm (green), and 24 μm (red) image of the Cygnus X region. White dots mark the locations of known massive binaries in Cygnus OB2. Magenta labels mark eclipsing massive binaries and their derived distances in kpc. Cyan labels denote radio parallax distance measurements toward masers from massive protostars (Rygl et al. 2012) and Schulte 5 (Dzib et al. 2012).

- Beerer, I. M., Koenig, X. P., Hora, J. L., et al. 2010, ApJ, 720, 679
 Bressan, A., Marigo, P., Girardi, L., Salasnich, B., Dal Cero, C.,
 Rubele, S., & Nanni, A. 2012, MNRAS, 427, 127B
 Caballero-Nieves, S. M., Nelan, E. P., Gies, D. R., et al. 2014, AJ, 147, 40
 Cardelli, J. A., Clayton, G. C., & Mathis, J. S. 1989, ApJ, 345, 245
 Comerón, F., Pasquali, A., Rodighiero, G., et al. 2002, A&A, 389, 874
 Comerón, F., & Pasquali, A. 2007, A&A, 467, L23
 Dame, T. M., & Thaddeus, P. 1985, ApJ, 297, 751
 Fitzpatrick, É. L., & Massa, D. 2007, ApJ, 663, 320
 Dame, T. M., Hartmann, D., & Thaddeus, P. 2001, ApJ, 547, 792
 Dzib, et al. 2012, arxiv:
 Drilling, J. S., & Landolt, A. U. 2000, in *Astrophysical Quantities*, ed. A. N. Cox (4th ed.; New York: Springer), 381
 González, J. F., Levato, H. 2006, A&A, 448, 283
 Gudehus, D. H. 2001, Bulletin of the American Astronomical Society, 33, 850
 Gvaramadze, V. V. 2007, A&A, 470, L9
 Hanson, M. M. 2003, ApJ, 597, 957

- Harnden, F. R., Jr., Branduardi, G., Gorenstein, P., et al. 1979, ApJ, 234, L51
 Hilditch, R. W. 2001, *An Introduction to Close Binary Stars*, by R. W. Hilditch, pp. 392. ISBN 0521241065. Cambridge, UK: Cambridge University Press, March 2001.
 Hillier, D. J., & Miller, D. L. 1998, ApJ, 496, 407
 Høg, E., Fabricius, C., Makarov, V. V., et al. 2000, A&A, 355, L27
 Hubeny, I., & Lanz, T. 1995, ApJ, 439, 875
 Jacoby, G. H., & Hunter, D. A. 1984, ApJS, 56, 257
 Johnson, H. L., & Morgan, W. W. 1954, ApJ, 119, 344
 Kennedy, M., Dougherty, S. M., Fink, A., & Williams, P. M. 2010, ApJ, 709, 632
 Kiminki, D. C., et al. 2007, ApJ, 664, 1120 (Paper I)
 Kiminki, D. C., McSwain, M. V., & Kobulnicky, H. A. 2008, ApJ, 679, 1478 (Paper II)
 Kiminki, D. C., Kobulnicky, H. A., Gilbert, I., Bird, S., Chunev, G. 2009, AJ, 137, 4608 (Paper III)
 Kiminki, D. C., Kobulnicky, H. A., Ewing, I., et al. 2012, ApJ, 747, 41 (Paper IV)
 Kiminki, D. C., & Kobulnicky, H. A. 2012, ApJ, 751, 4 (Paper V)
 Knödlseder, J. 2000, A&A, 360, 539
 Kobulnicky, H. A., & Fryer, C. L. 2007, ApJ, 670, 747

- Kobulnicky, H. A., Gilbert, I. J., & Kiminki, D. C. 2010, ApJ, 710, 549
- Kobulnicky, H. A., Kiminki, D., Lundquist, M., et al. 2014, ApJ, 213, 34
- Kobulnicky, H. A., Smullen, R. A., Kiminki, D. C., et al. 2012, ApJ, 756, 50
- Kobulnicky, H. A., Lundquist, M. J., Bhattacharjee, A., & Kerton, C. R. 2012, AJ, 143, 71
- Kurucz, R. L. 1979, ApJS, 40, 1
- Kurucz, R. L. 1992, The Stellar Populations of Galaxies, 149, 225
- Lanz, T., & Hubeny, I. 2003, ApJS, 146, 417
- Lanz, T., & Hubeny, I. 2007, ApJS, 169, 83
- Leung, H. O., & Thaddeus, P. 1992, ApJS, 81, 267
- Linder, N., Rauw, G., Manfroid, J., et al. 2009, A&A, 495, 231
- Linder, N., Rauw, G., Sana, H., De Becker, M., & Gosset E. 2007, A&A, 474, 1
- Lucas, P. W., Hoare, M. G., Longmore, A., et al. 2008, MNRAS, 391, 136
- Markwardt, C. B. 2009, Astronomical Data Analysis Software and Systems XVIII, 411, 251
- Martins, F., Schaefer, D., & Hillier, D. J. 2002, A&A, 382, 999
- Martins, F., Schaefer, D., & Hillier, D. J. 2005, A&A, 436, 1049
- Massey, P., & Thompson, A. B. 1991, AJ, 101, 1408
- McLaughlin, D. B. 1924, ApJ, 60, 22
- Motte, F., Bontemps, S., Schilke, P., et al. 2007, A&A, 476, 1243
- Münch, L., & Morgan, W. W. 1953, ApJ, 118, 161
- Nazé, Y., Mahy, L., Damerdji, Y., et al. 2012, A&A, 546, A37
- Nelder, J. A., & Mead, R. 1965, Computer Journal, 7, 308
- Nicolet, B. 1978, A&AS, 34, 1
- O'Connell, D. J. K. 1951, Publ. Riverview College Obsr., 2, 85
- Odenwald, S. F., & Schwartz, P. R. 1993, ApJ, 405, 706
- Otero, S. 2008a, Open European Journal on Variable Stars, 83, 1
- Piddington, J. H., & Minnett, H. C. 1952, Australian Journal of Scientific Research A Physical Sciences, 5, 17
- Prša, A., & Zwitter, T. 2005, ApJ, 628, 426
- Puls, J., Vink, J. S., & Najarro, F. 2008, A&A Rev., 16, 209
- Reddish, V. C., Lawrence, L. C., & Pratt, N. M. 1966, Publications of the Royal Observatory of Edinburgh, 5, 111
- Rios, L. Y., & DeGioia-Eastwood, K. 2004, BAAS, 205, No. 09.05
- Roberts, D. H., Lehár, J., & Dreher, J. W. 1987, AJ, 93, 968
- Rossiter, R. A. 1924, ApJ, 60, 15
- Rygl, K. L. J., Brunthaler, A., Sanna, A., et al. 2012, A&A, 539, A79
- Schneider, N., Bontemps, S., Simon, R., et al. 2006, A&A, 458, 855
- Schulte, D. H. 1956, ApJ, 124, 530
- Schulte, D. H. 1958, AJ, 128, 41
- Souza, S. P., Beltz-Mohrmann, G., & Sami, M. 2014, JAAVSO, 42, 154
- Stroud, V. E., Clark, J.S., Negueruela, I., Roche, P., & Norton, A.J. 2009, A&A, 511, 84
- Torres-Dodgen, A. V., Carroll, M., & Tapia, M. 1991, MNRAS, 249, 1
- Turner, D. G. 1989, AJ, 98, 2300
- van Hamme, W. 1993, AJ, 106, 2096
- Vargas-Alvarez, C., Kobulnicky, H. A., et al., 2013, ApJ, 145, 125
- Walborn, N. R. 1973, ApJ, 180, 35
- Walborn, N. R. 1980, ApJS, 44, 535
- Walborn, N. R., & Fitzpatrick, E. L. 1990, PASP, 102, 379
- Waldron, W. L., Corcoran, M. F., Drake, S. A., & Smale, A. P. 1998, ApJS, 118, 217
- Woźniak, P. R., Vestrand, C. W., Akerlof, C. W., et al. 2004, ApJ, 127, 2436
- Wendker, H. J., Higgs, L. A., & Landecker, T. L. 1991, A&A, 241, 551
- Wilson, R. E., & Devinney, E. J. 1971, ApJ, 166, 605
- Wright, N. J., Drew, J. E., & Mohr-Smith, M. 2014, MNRAS, 449, 741
- Yaşarsoy, B., & Yakut, K. 2012, AJ, 145, 9
- Yaşarsoy, B., & Yakut, K. 2014, New Astronomy, 31, 32
- Zhang, B., Reid, M. J., Menten, K. M., Zheng, X. W., & Brunthaler, A. 2012, A&A, 544, A42

APPENDIX

TABLE A.1
RADIAL VELOCITIES FOR MT91 372 & MT91 696

Date (HJD-2,400,000)	ϕ	V_{r1} (km s $^{-1}$)	$O_1 - C_1$ (km s $^{-1}$)	V_{r2} (km s $^{-1}$)	$O_2 - C_2$ (km s $^{-1}$)
MT91 372					
54,754.643.....	0.633	79.8 (14.2)	-16.5	-258.2 (14.4)	-19.0
54,756.629.....	0.124	19.4 (17.2)	3.1
54,758.616.....	0.416	-72.0 (21.8)	5.2	181.5 (36.2)	28.5
56,437.744.....	0.237	-139.2 (8.9)	-2.4	295.8 (11.5)	5.9
56,438.831.....	0.725	96.8 (10.0)	-26.8	-278.5 (17.6)	23.8
56,439.755.....	0.140	-120.1 (10.2)	-17.9	221.6 (13.8)	10.0
56,440.777.....	0.199	71.1 (9.9)	-4.5	-177.4 (12.3)	14.8
56,445.838.....	0.871	77.9 (5.7)	-5.3	-208.1 (9.5)	2.9
56,446.752.....	0.281	-150.7 (9.0)	-12.8	306.0 (12.4)	13.8
56,458.825.....	0.701	127.0 (12.7)	6.4	-269.4 (15.6)	26.0
56,459.828.....	0.151	-122.3 (8.2)	-14.1	242.6 (11.6)	17.5
56,466.865.....	0.311	-137.2 (8.1)	-4.6	273.7 (12.5)	-6.1
MT91 696					
54,699.741.....	0.288	-234.4 (9.2)	7.0	302.9 (14.8)	-0.4
54,700.772.....	0.990	-4.9 (12.3)	-22.2	11.5 (15.5)	30.6
54,700.902.....	0.078	-139.4 (22.9)	-23.0	150.1 (27.6)	2.7
54,701.703.....	0.623	187.9 (7.3)	12.4	-233.9 (13.7)	-17.7
54,701.910.....	0.764	249.1 (9.4)	-0.4	-319.9 (13.6)	-11.3
54,724.617.....	0.220	-247.4 (5.1)	-3.5	300.0 (8.6)	-6.4
54,724.728.....	0.295	-235.5 (8.8)	2.7	296.5 (10.9)	-2.8
54,724.824.....	0.360	-178.1 (19.4)	12.6	225.5 (29.0)	-14.5
54,725.609.....	0.895	129.0 (6.1)	-25.2	-166.7 (8.3)	23.0
54,725.736.....	0.981	3.5 (8.8)	-26.9	17.3 (10.6)	52.8
54,725.854.....	0.061	-114.5 (7.8)	-21.7	122.5 (9.8)	4.4
54,726.629.....	0.189	137.4 (6.5)	4.1	-181.4 (11.9)	-17.8
54,726.743.....	0.667	218.0 (7.3)	0.4	-282.9 (9.8)	-14.1
54,726.842.....	0.734	255.4 (16.8)	6.3	-318.7 (21.9)	-10.6
54,729.629.....	0.631	190.0 (6.6)	6.2	-257.7 (10.1)	-31.1
54,729.724.....	0.696	242.2 (5.9)	6.2	-302.2 (7.8)	-10.1
54,729.813.....	0.757	255.0 (6.9)	4.8	-297.6 (8.8)	11.7
56,218.613.....	0.111	-162.4 (8.9)	-3.0	200.1 (11.5)	-0.9

TABLE A.1 — *Continued*

Date (HJD-2,400,000)	ϕ	V_{r1} (km s $^{-1}$)	$O_1 - C_1$ (km s $^{-1}$)	V_{r2} (km s $^{-1}$)	$O_2 - C_2$ (km s $^{-1}$)
56,222.568.....	0.803	231.6 (5.9)	-5.1	-280.3 (8.2)	12.2
56,218.632.....	0.124	-167.3 (10.9)	7.2	242.6 (13.7)	22.8
56,222.788.....	0.953	62.6 (7.9)	-11.1	-85.1 (11.8)	4.3
CPR2002 A36					
54,403.610.....	0.162	-153.8 (7.1)	5.3	177.8 (4.2)	1.6
54,403.702.....	0.181	-167.8 (6.7)	-2.3	193.8 (3.9)	2.8
54,405.705.....	0.610	9.9 (15.4)	-55.3	-208.5 (9.1)	-20.3
54,406.632.....	0.808	110.2 (4.8)	-0.1	-257.5 (2.9)	-9.0
54,406.757.....	0.835	104.7 (6.2)	2.2	-243.7 (3.7)	-10.7
54,408.664.....	0.243	-185.7 (11.0)	-12.0	234.9 (6.5)	20.7
54,409.730.....	0.471	-39.9 (48.9)	16.0	-14.5 (28.8)	-50.6
54,410.667.....	0.671	90.8 (7.1)	-7.9	-245.0 (4.2)	-7.8
54,414.827.....	0.119	-100.3 (10.2)	38.4	121.2 (6.0)	-11.2
54,642.754.....	0.317	-176.2 (7.1)	-15.7	211.5 (4.2)	16.8
54,644.770.....	0.748	116.9 (9.1)	1.0	-252.1 (5.4)	10.3
54,645.834.....	0.976	-25.6 (6.0)	47.4
54,647.767.....	0.389	-148.2 (11.5)	-25.1	115.4 (6.8)	-19.8
54,669.843.....	0.112	-103.4 (8.7)	31.7	121.5 (5.1)	-2.0
54,672.777.....	0.739	109.5 (7.2)	-5.6	-276.0 (4.2)	-14.3
54,673.875.....	0.974	-62.3 (27.4)	13.3
54,696.684.....	0.853	121.3 (6.8)	26.4	-229.1 (4.0)	-9.7
54,696.964.....	0.913	101.5 (8.0)	37.1	-158.7 (4.7)	-0.6
54,697.659.....	0.062	-68.8 (19.5)	37.4	14.0 (11.5)	-41.6
54,698.753.....	0.296	-196.2 (11.4)	-29.5	206.3 (6.7)	1.0
54,700.871.....	0.749	103.6 (9.0)	-12.4	-259.7 (5.3)	2.7
54,701.895.....	0.968	-78.4 (29.5)	6.3
Schulte 3					
53,989.652.....	0.643	42.1 (5.7)	15.6	-224.4 (3.4)	0.4
53,989.774.....	0.668	37.4 (4.1)	3.4	-238.6 (3.4)	5.8
53,990.848.....	0.895	16.3 (7.2)	-0.8	-191.9 (4.0)	-3.5
54,286.904.....	0.276	-145.4 (8.3)	-7.2	201.2 (8.4)	28.0
54,341.802.....	0.843	117.2 (12.3) ^a	82.6	-217.4 (5.4)	19.1
54,342.724.....	0.038	5.0 (104.8) ^a	82.0	13.1 (46.0)	8.1
54,343.830.....	0.271	-134.0 (6.0) ^a	4.7	249.3 (2.6) ^a	75.2
54,344.761.....	0.467	-21.1 (36.4) ^a	46.2	11.0 (16.0)	1.0
54,345.781.....	0.682	90.1 (9.8) ^a	53.0	-251.2 (4.3)	1.5
54,346.787.....	0.894	54.5 (25.4) ^a	37.0	-170.1 (11.1)	19.3
54,347.755.....	0.098	-19.0 (9.7) ^a	89.8	101.4 (4.3)	19.3
54,348.840.....	0.326	-116.8 (5.7) ^a	13.1	220.4 (2.5) ^a	66.8
54,628.748.....	0.305	-128.3 (4.7)	6.1	172.4 (5.8)	8.0
54,628.880.....	0.333	-134.2 (4.0)	-5.8	162.7 (3.3)	13.1
54,629.866.....	0.141	-49.7 (3.3)	-26.8	-126.7 (3.2)	-16.7
54,630.739.....	0.725	32.5 (4.4)	-11.1	-260.6 (2.6)	8.7
54,630.852.....	0.749	40.2 (4.1)	-4.8	-258.6 (2.8)	13.5
54,632.745.....	0.147	-122.1 (4.5)	4.7	155.4 (4.5)	24.2
54,633.741.....	0.357	-140.0 (5.6)	-18.9	128.0 (5.9)	-3.7
54,633.859.....	0.382	-120.0 (3.0)	-8.3	82.9 (3.6)	-26.7
54,642.717.....	0.249	-128.9 (6.4) ^a	10.9	258.2 (2.8) ^a	82.9
54,642.878.....	0.283	-143.6 (3.8) ^a	-6.1	252.9 (1.7) ^a	81.0
54,644.684.....	0.663	91.2 (6.4) ^a	58.6	-254.0 (2.8)	-13.3
54,645.734.....	0.884	101.5 (13.8) ^a	80.3	-188.2 (6.1)	11.6
54,646.707.....	0.089	-39.9 (8.9) ^a	65.3	100.8 (3.9)	28.7
54,647.688.....	0.296	-139.1 (8.0) ^a	-3.2	229.0 (3.5) ^a	61.2
54,648.902.....	0.152	-13.9 (12.1) ^a	2.6	-115.8 (5.3)	10.0
54,672.692.....	0.165	0.3 (5.9) ^a	9.6	-142.7 (2.6)	-0.1
56,218.402.....	0.257	-124.8 (8.0) ^a	14.6	223.8 (3.5) ^a	47.4
56,219.341.....	0.455	-56.1 (51.0) ^a	17.5	-22.7 (22.4)	-48.4
56,222.349.....	0.089	-81.9 (7.9) ^a	24.0	172.7 (3.5) ^a	98.1

^a Observation not used in solution fit.

TABLE A.2
V-BAND PHOTOMETRY OF MT91 372

HJD-2,400,000 (days)	V (mag)	σ^a (mag)
56,458.819.....	14.983	0.011
56,458.821.....	14.991	0.012
56,458.822.....	14.936	0.011
56,458.825.....	14.955	0.011
56,458.827.....	14.962	0.011
56,458.830.....	14.977	0.011
56,458.832.....	14.993	0.011
56,458.837.....	14.986	0.011
56,458.839.....	14.994	0.011
56,458.841.....	14.964	0.011

NOTE. — Table A.2 is published in its entirety in the electronic edition of the *Astrophysical Journal*. A portion is shown here for guidance regarding its form and content.

^a 1 σ error includes formal photon statistics uncertainties only; additional uncertainties at the level of 0.01 mag are present as a result of uncorrected atmospheric transparency variations.

TABLE A.3
V-BAND PHOTOMETRY OF MT91 696

HJD-2,400,000 (days)	V (mag)	σ^a (mag)
56,219.567.....	12.066	0.002
56,219.569.....	12.068	0.002
56,219.570.....	12.064	0.002
56,219.572.....	12.067	0.002
56,219.573.....	12.067	0.002
56,219.589.....	12.065	0.002
56,219.590.....	12.069	0.002
56,219.592.....	12.063	0.002
56,219.593.....	12.067	0.002
56,219.595.....	12.069	0.002

NOTE. — MT91 696 photometry includes the contribution from the blended 0.⁰02 tertiary MT91 696c discussed in the text. Table A.3 is published in its entirety in the electronic edition of the *Astrophysical Journal*. A portion is shown here for guidance regarding its form and content.

^a 1 σ error includes formal photon statistics uncertainties only; additional uncertainties at the level of 0.01 mag are present as a result of uncorrected atmospheric transparency variations.

TABLE A.4
V-BAND PHOTOMETRY OF CPR2002 A36

HJD-2,400,000 (days)	V (mag)	σ^a (mag)
56,271.541.....	11.421	0.002
56,271.542.....	11.432	0.002
56,271.543.....	11.428	0.002
56,271.648.....	11.447	0.002
56,271.649.....	11.434	0.002
56,271.649.....	11.429	0.002
56,271.650.....	11.435	0.002
56,271.650.....	11.428	0.002
56,271.651.....	11.430	0.002
56,271.651.....	11.439	0.002

NOTE. — Table A.4 is published in its entirety in the electronic edition of the *Astrophysical Journal*. A portion is shown here for guidance regarding its form and content.

^a 1 σ error includes formal photon statistics uncertainties only; additional uncertainties at the level of 0.01 mag are present as a result of uncorrected atmospheric transparency variations.

TABLE A.5
V-BAND PHOTOMETRY OF SCHULTE 3

HJD-2,400,000 (days)	V (mag)	σ^a (mag)
56,218.586.....	10.194	0.001
56,218.587.....	10.182	0.001
56,218.587.....	10.169	0.001
56,218.588.....	10.168	0.001
56,218.588.....	10.171	0.001
56,218.589.....	10.175	0.001
56,218.589.....	10.181	0.001
56,218.590.....	10.156	0.001
56,218.590.....	10.174	0.001
56,218.591.....	10.149	0.001

NOTE. — Schulte 3 photometry includes the contribution from the blended tertiary Schulte 3C discussed in the text. Table A.5 is published in its entirety in the electronic edition of the *Astrophysical Journal*. A portion is shown here for guidance regarding its form and content.

^a 1 σ error includes formal photon statistics uncertainties only; additional uncertainties at the level of 0.01 mag are present as a result of uncorrected atmospheric transparency variations.